

**NASA TECHNICAL
MEMORANDUM**



NASA TM X-2816

NASA TM X-2816

**FLIGHT-MEASURED X-24A LIFTING BODY
CONTROL-SURFACE HINGE MOMENTS AND
CORRELATION WITH WIND-TUNNEL PREDICTIONS**

by Ming H. Tang and George P. E. Pearson

Flight Research Center

Edwards, Calif. 93523

NATIONAL AERONAUTICS AND SPACE ADMINISTRATION • WASHINGTON, D. C. • JUNE 1973

1. Report No. NASA TM X-2816		2. Government Accession No.		3. Recipient's Catalog No.	
4. Title and Subtitle FLIGHT-MEASURED X-24A LIFTING BODY CONTROL-SURFACE HINGE MOMENTS AND CORRELATION WITH WIND-TUNNEL PREDICTIONS				5. Report Date June 1973	
				6. Performing Organization Code	
7. Author(s) Ming H. Tang and George P. E. Pearson				8. Performing Organization Report No. H-748	
				10. Work Unit No. 756-47-01-00-24	
9. Performing Organization Name and Address NASA Flight Research Center P. O. Box 273 Edwards, California 93523				11. Contract or Grant No.	
				13. Type of Report and Period Covered Technical Memorandum	
12. Sponsoring Agency Name and Address National Aeronautics and Space Administration Washington, D. C. 20546				14. Sponsoring Agency Code	
15. Supplementary Notes					
16. Abstract <p style="text-align: center;">Control-surface hinge-moment measurements obtained in the X-24A lifting body flight-test program are compared with results from wind-tunnel tests. The effects of variations in angle of attack, angle of sideslip, rudder bias, rudder deflection, upper-flap deflection, lower-flap deflection, Mach number, and rocket-engine operation on the control-surface hinge moments are presented.</p> <p style="text-align: center;">In-flight motion pictures of tufts attached to the inboard side of the right fin and the rudder and upper-flap surfaces are discussed.</p>					
17. Key Words (Suggested by Author(s)) X-24A lifting body vehicle Flight-test and wind-tunnel hinge moments Flow visualization				18. Distribution Statement Unclassified - Unlimited	
19. Security Classif. (of this report) Unclassified		20. Security Classif. (of this page) Unclassified		21. No. of Pages 37	
				22. Price* \$3.00	

FLIGHT-MEASURED X-24A LIFTING BODY CONTROL-SURFACE
HINGE MOMENTS AND CORRELATION WITH WIND-TUNNEL PREDICTIONS

Ming H. Tang and George P. E. Pearson
Flight Research Center

INTRODUCTION

The concept of maneuverable vehicles capable of controlled reentry from earth orbit to a tangential landing led to the construction of three manned lifting body vehicles of different configurations to investigate the terminal portion of flight below a Mach number of approximately 2.0 (ref. 1). Because the configurations were different from those of conventional aircraft, there was little design precedent upon which to rely. In the structural design of the lifting body vehicles, the predictions of airloads were based more heavily on configurational test results than for most flight vehicles. The final configurations were the products of an evolutionary process based on the results of numerous wind-tunnel tests. Therefore, designers of future lifting body vehicles would benefit greatly from knowing the magnitude of aerodynamic loads experienced during flight and how those loads compare with values predicted from wind-tunnel measurements.

As part of the lifting body flight-test program at the NASA Flight Research Center, detailed aerodynamic loads studies (refs. 2 to 4) were made on each of the three lifting body vehicles, the M2-F2, HL-10, and X-24A. This report presents the control-surface hinge moments obtained in the X-24A flight-test program and compares these values with results from wind-tunnel tests reported in references 5 to 8. In addition, in-flight motion pictures of tufts attached to the inboard side of the right fin and the rudder and upper-flap surfaces are discussed.

SYMBOLS

Physical quantities in this report are given in the International System of Units (SI) and parenthetically in U.S. Customary Units. The measurements were taken in U.S. Customary Units. Details concerning the use of SI, together with physical constants and conversion factors, are given in reference 9.

C_h	control-surface hinge-moment coefficient, $\frac{H}{qS\bar{c}}$
\bar{c}	average chord, m (in.)
H	hinge moment, m-N (in-lb)
M	free-stream Mach number
q	free-stream dynamic pressure, N/m^2 (lb/ft ²)

S	surface area, m ² (ft ²)
V	relative wind velocity, m/sec (ft/sec)
α	true angle of attack, deg
β	angle of sideslip, deg
δ	control-surface deflection, deg

Subscripts:

l	lower flap
r	rudder
rb	rudder bias
rl	lower rudder
ru	upper rudder
u	upper flap

FLIGHT-TEST VEHICLE

A photo of the X-24A research vehicle is shown in figure 1(a). The X-24A has a boattailed body with a thick midsection and a blunt nose, three stabilizing vertical fins, and eight control surfaces—four rudders and four flaps. A three-view drawing of the vehicle is shown in figure 1(b).

To provide directional stability, the two pairs of rudders at the rear portion of the outboard fins were moved symmetrically in bias with their trailing edges deflected either outward or inward from the zero position by an equal amount. Figure 2(a) shows the rudders at -10° bias and figure 2(b), at 0° bias. To provide directional control, the two upper rudders were deflected in unison (both moved in the same direction) from the bias position. For pitch and trim control the two upper flaps and the two lower flaps were deflected symmetrically. For roll control either the upper flaps or the lower flaps were deflected differentially.

Pertinent physical dimensions of the fins and control surfaces are listed in table 1. Additional physical details of the X-24A vehicle are given in reference 7.

The sign convention for the X-24A control-surface hinge moments and deflections is shown in figure 3.

INSTRUMENTATION

Flight data were obtained with a pulse code modulation (PCM) data acquisition system. The system converted analog signals from the sensor to digital format and telemetered the digitized data to a ground station for recording on magnetic tape on a time-sharing basis.

The upper-rudder hinge moments were obtained with standard four-active-arm axial-force strain-gage bridges mounted on push-pull rods. The lower-rudder and the upper-flap and lower-flap hinge moments were obtained with four-active-arm bending-moment strain-gage bridges mounted on the actuator horn assemblies of these surfaces.

The hinge-moment instrumentation was calibrated by loading each surface in place on the vehicle at three positions. The strain-gage outputs were conditioned through an onboard PCM system, wired to a ground station, and recorded on magnetic tape. Data from the calibration were then used in a computer program to calculate the control-surface hinge-moment coefficients.

The position of each control surface was measured with a control-position transducer which was calibrated in place on the vehicle with a template before each flight.

Mach number and dynamic pressure were measured with a standard NASA air-speed head, described in reference 10. Angle of attack and angle of sideslip were measured with vanes mounted on the nose boom of the vehicle, as shown in figure 1.

ESTIMATED ERRORS

Estimates were made of the errors in each of the parameters pertinent to the presentation of the hinge-moment data. The estimates include sensor, calibration, and data reduction errors. The hinge-moment errors were obtained from reference 5. Angle-of-attack corrections are given in Air Force Flight Test Center Technology Document No. 71-8 by Lawrence G. Ash. Angle-of-sideslip errors were considered to be insignificant, thus no corrections were made to the flight-measured angles of sideslip.

Estimated errors in the pertinent vehicle and hinge-moment parameters are:

α , deg	± 0.65
β , deg	± 0.33
q , N/m^2 (lb/ft^2)	± 96 (± 2)
M	± 0.01
δ_1 , deg	± 0.43
δ_u , deg	± 0.65

δ_{rl} , deg	± 0.23
δ_{ru} , deg	± 0.54
H_l , m-N (in-lb)	± 29.4 (± 260)
H_u , m-N (in-lb)	± 14.1 (± 125)
H_{rl} , m-N (in-lb)	± 8.6 (± 76)
H_{ru} , m-N (in-lb)	± 5.8 (± 51)

FLIGHT-TEST PROGRAM

Ten unpowered and 18 rocket-powered research flights were made with the X-24A vehicle. The vehicle was air-launched from a modified B-52 carrier airplane at altitudes of 12,192 meters to 14,326 meters (40,000 feet to 47,000 feet) and at Mach numbers of 0.59 to 0.73. Longitudinal and lateral-directional maneuvers were performed to investigate the subsonic, transonic, and supersonic flight characteristics. The longitudinal maneuvers consisted of pushover-pullups and pitch pulses, and the lateral-directional maneuvers were lateral perturbations initiated by a sharp rudder doublet, followed by a stick-fixed vehicle oscillation, and terminated with a sharp aileron doublet. The vehicle angle of attack varied between 0° and 20° , and the Reynolds number ranged from 12.5×10^6 to 65×10^6 , based on the vehicle reference length of 7.01 meters (23 feet). The maximum Mach number attained was 1.60, and the peak altitude was 21,763 meters (71,400 feet). The maximum control-surface hinge moments experienced in flight and the design-limit hinge moments are presented in table 2.

WIND-TUNNEL TESTS

The small-scale wind-tunnel hinge moments were obtained on an 8-percent-scale, steel X-24A (SV-5P) pressure model in the NASA Langley Research Center's 8-foot transonic pressure tunnel (ref. 6), the Cornell Aeronautical Laboratory's 8-foot wind tunnel (ref. 7), and the North American 7 x 7 foot transonic wind tunnel (ref. 8). The full-scale hinge moments were measured on the flight-test vehicle in the NASA Ames Research Center's 40- by 80-Foot Tunnel (ref. 5).

RESULTS AND DISCUSSION

Control-Surface Hinge-Moment Coefficients

Flight-determined variations of the left control-surface hinge-moment coefficients with angle of attack, angle of sideslip, control-surface deflection, rocket-engine operation, and Mach number are presented in figures 4 to 12 and compared with data

obtained from references 5 to 8.

The effect of changes in rudder bias and angle of attack at a Mach number of 0.6 on the control-surface hinge-moment coefficients is shown in figure 4. The greatest increase in the upper-rudder hinge-moment coefficient and the lower-rudder hinge-moment coefficient is attributed to the change in rudder bias from -10° to 0° (figs. 4(a) and 4(b)). This change in rudder bias lowers the value of the upper-flap hinge-moment coefficient and has essentially no effect on the lower-flap hinge-moment coefficient (figs. 4(c) and 4(d)). In general, an increase in angle of attack increases the value of the upper- and lower-rudder hinge-moment coefficients and has virtually no effect on the upper- or lower-flap hinge-moment coefficients. Figures 4, 5, and 6 indicate that the lower-rudder hinge-moment coefficient remains fixed at zero load for angles of attack less than 12° at $M = 0.6$ and $\delta_{rb} = 0^\circ$.

The wind-tunnel and flight upper-rudder hinge-moment coefficients at both rudder-bias positions correlate well (fig. 4(a)). The wind-tunnel hinge-moment coefficients for the lower rudder (fig. 4(b)), upper flap (fig. 4(c)), and lower flap (fig. 4(d)) are slightly larger than the flight results throughout the angle-of-attack range investigated.

Figure 5 shows the effect of upper-flap deflection and angle-of-attack variation at $M = 0.6$ on the control-surface hinge-moment coefficients. An increase in the upper-flap deflection decreases the upper-rudder hinge-moment coefficient (fig. 5(a)), increases the upper-flap hinge-moment coefficient (fig. 5(c)), and has little effect on the lower-rudder or lower-flap hinge-moment coefficients (figs. 5(b) and 5(d)).

The wind-tunnel upper-rudder hinge-moment coefficient changes less with upper-flap deflection than the flight hinge-moment coefficient (fig. 5(a)). Also, the wind-tunnel lower-rudder hinge-moment coefficient decreases with increase in upper-flap deflection at angles of attack greater than 8° (fig. 5(b)). Although the magnitude of the wind-tunnel upper-flap hinge-moment coefficient is slightly larger than that of the flight data, the increase with upper-flap deflection is the same (fig. 5(c)).

The effect of lower-flap deflection at $M = 0.6$ on the control surface hinge-moment coefficients is shown in figure 6. Variation in the lower-flap position has virtually no effect on the upper- or lower-rudder hinge-moment coefficients (figs. 6(a) and 6(b)). The wind-tunnel upper-rudder hinge-moment-coefficient data show excellent agreement with the flight values. The wind-tunnel lower-rudder hinge-moment-coefficient data were higher than the flight values. An increase in the lower-flap deflection increases the lower-flap hinge-moment coefficient (fig. 6(d)) and slightly increases the upper-flap coefficient (fig. 6(c)). The wind-tunnel lower-flap hinge-moment coefficient is again slightly higher in magnitude than the flight hinge-moment coefficient as well as in the incremental increase due to lower-flap deflection.

The effect of rocket-engine operation at Mach numbers of 0.9 and 1.2 on the control-surface hinge moments is shown in figures 7 and 8, respectively. The engine-off hinge-moment values are compared with wind-tunnel values from reference 7. The upper-flap hinge-moment coefficient shows a notable decrease due to rocket-engine operation at $M = 1.2$; this effect is most apparent at low

angles of attack (fig. 8(c)). Coefficients for the other control surfaces show no significant change as a result of engine operation. In general, the wind-tunnel values at Mach numbers of 0.9 and 1.2 agree well with the engine-off flight results, except for the lower-flap values at $M = 1.2$ (fig. 8(d)).

Control-surface hinge-moment coefficients as a function of Mach number are shown in figure 9. The surfaces all indicate an increase in hinge moment at transonic speeds; however, the lower-rudder hinge-moment coefficient shows a negative slope with respect to Mach number up to 0.9 (fig. 9(b)).

In general, the wind-tunnel rudder hinge moments from references 5, 7, and 8 show good agreement with the flight values (figs. 9(a) and 9(b)) except for the upper-rudder hinge-moment coefficient at Mach numbers greater than 1.1. The wind-tunnel values of the upper-flap hinge-moment coefficient are slightly higher than the flight results except at transonic speeds (fig. 9(c)). The flight and wind-tunnel values of the lower-flap hinge-moment coefficient agree well at Mach numbers less than 1.1 (fig. 9(d)). At higher speeds, the flight data are significantly lower than the wind-tunnel values.

The effect of rudder deflection on the upper- and lower-rudder hinge-moment coefficients is shown in figure 10 for Mach numbers of 0.5 to 1.4. Both the flight and wind-tunnel values indicate an increase in rudder hinge-moment coefficient with rudder deflection.

The flight values of $\frac{\partial C_{h_{ru}}}{\partial \delta_r}$ show fair correlation with the wind-tunnel results from reference 7 except at transonic speeds, where the flight values are lower than the wind-tunnel predictions (fig. 10(a)). Although rudder deflection has a relatively small effect on the lower-rudder hinge moment, the flight values of $\frac{\partial C_{h_{rl}}}{\partial \delta_r}$ show excellent correlation with the wind-tunnel values throughout the Mach range investigated (fig. 10(b)).

Figure 11 shows the effect of angle of sideslip on the upper- and lower-rudder and upper-flap hinge-moment coefficients. An increase in negative sideslip angle increases the upper- and lower-rudder hinge-moment coefficients (figs. 11(a) and 11(b)). An increase in positive sideslip angle increases the upper-flap hinge-moment coefficient at Mach numbers greater than 0.6 (fig. 11(c)). Also, $\frac{\partial C_{h_u}}{\partial \beta}$ increases with increasing Mach number.

In general, the flight values of $\frac{\partial C_{h_{ru}}}{\partial \beta}$ and $\frac{\partial C_{h_{rl}}}{\partial \beta}$ show fair agreement with the wind-tunnel data from reference 7 (figs. 11(a) and 11(b)). However, the flight

values of $\frac{\partial C_{h_u}}{\partial \beta}$ are generally smaller than the wind-tunnel values (fig. 11(c)).

The effect of lower-flap deflection on the lower-flap hinge-moment coefficient at Mach numbers of 0.5 to 1.5 is shown in figure 12. The wind-tunnel values from reference 7 are consistently higher than the flight values and show a notable increase at transonic speeds that is not evident in the flight results.

Flow Visualization

During the first phase of the X-24A flight-test program, a mild, high-frequency buffet was reported by the pilot and was also evident in the accelerometer and rudder hinge-moment data. To investigate the flow characteristics in this region and thus better define this flow phenomenon, tufts were affixed to the inboard surface of the right fin, including the two rudder surfaces, and to the right upper flap. Motion pictures of the tufts were taken during 14 flights (glide and powered) with a 16-mm camera mounted on the center fin.

Analysis of the films revealed three distinct flow patterns, chordwise, spanwise, and separated, on the inboard surface of the fin, as shown in figures 13(a) to 13(c). The flow was considered to be chordwise when the tufts were alined with the reference marks or angled no greater than 30° from the reference marks, spanwise when the tuft angles exceeded 45° from the reference marks, and separated when the tufts showed no specific directional alinement, that is, random motion.

The chordwise and the spanwise flows were also classified as steady and unsteady. The flow was considered to be steady when the tufts remained alined in a given direction with virtually no oscillatory motion, and unsteady when the tufts remained alined in a general direction but oscillated at a high frequency. Figure 14 shows that the flow over the aft region of the upper flap was steady chordwise. For the conditions investigated, this pattern remained constant and appeared to be independent of vehicle attitudes and control-surface deflections.

A typical time history of the right control-surface hinge-moment strain-gage responses is shown in figure 15. The abrupt increase in peak-to-peak amplitudes of the upper- and lower-rudder hinge moments correlates with changes shown in the tuft motion pictures, indicating the onset of unsteady spanwise and separated flow over the fin. The average level of the hinge moments remained virtually constant. The upper- and the lower-flap hinge-moment data showed no significant change in peak-to-peak amplitudes, and the tuft motion pictures indicated no change in flow over the upper flap.

Figure 16 shows the types of flow over the inboard surface of the right fin and upper flap, as determined from tuft photos. At $\delta_u = -12^\circ$, $\delta_{rb} = -10^\circ$, and $M = 0.4$ to 0.6, the flow is steady chordwise throughout the region at $\alpha = 5^\circ$ (fig. 16(a)). The flow changes to steady spanwise over the upper part of the fin at $\alpha = 10^\circ$ (fig. 16(b)). At $\delta_u = -40^\circ$, $\delta_{rb} = 0^\circ$, and $M = 0.9$ to 1.3, the flow on the top and bottom regions of the fin is unsteady spanwise and on the mid-region is unsteady chordwise at $\alpha = 5^\circ$ (fig. 16(c)). At $\alpha = 10^\circ$ the flow becomes separated over the upper portion of the fin; over the bottom portion it becomes unsteady spanwise

(fig. 16(d)). The flow over the upper flap remains steady chordwise (figs. 16(a) to 16(d)).

The parameters that affected the flow, as indicated by the tuft films, were angle of attack, Mach number, and upper-flap position. Although figure 16 is restricted to a few specific flight conditions, in general, the tuft photos showed that the flow on the inboard side of the fin changed from steady chordwise to unsteady spanwise, then separated with increasing angle of attack. The transition angle of attack at which the flow changed decreased with increasing Mach number up to 0.7. At Mach numbers greater than 0.7, the flow was not visibly affected by changes in angle of attack or Mach number and was predominantly spanwise.

The tuft movies also showed that as upper-flap deflection increased, the flow changed from chordwise to spanwise over the inboard surface of the fin and rudders.

For the angle-of-attack and Mach number range investigated, the trend of the flow separation over the inner surface of the right fin and the rudder surfaces indicated by flight rudder hinge-moment data in previously mentioned AFFTC TD-71-8 and wind-tunnel rudder inboard trailing-edge pressure divergence data in reference 7 was the same as that shown in the flight tuft motion pictures.

CONCLUDING REMARKS

Control-surface hinge moments obtained during the X-24A lifting body flight-test program were compared with wind-tunnel test results. In general, the agreement was good.

The upper- and the lower-rudder hinge moments increased with increase in rudder bias from -10° to 0° , rudder deflection, angle of attack, and angle of sideslip. Rocket-engine operation had virtually no effect on the rudder hinge moments. Both the upper- and lower-rudder hinge moments indicated an increase in hinge moment at transonic speeds.

The upper-flap hinge moment decreased with increasing rudder bias from -10° to 0° and increased with upper-flap deflection. The upper-flap hinge-moment coefficient decreased notably with rocket-engine operation at a free-stream Mach number of 1.2. The upper-flap hinge moment was also sensitive to changes in angle of sideslip, particularly at transonic speeds.

Both the upper- and the lower-flap hinge moments indicated an increase in hinge moment at transonic speeds.

The lower-flap hinge moment increased primarily with increase in lower-flap deflection and was unaffected by rocket-engine operation.

In-flight motion pictures of tufts attached to the inboard side of the right fin and the rudder and upper-flap surfaces indicated a flow pattern sensitivity to angle of attack, Mach number, and upper-flap position, particularly at Mach numbers below 0.7; at Mach numbers greater than 0.7, a predominance of spanwise flow was indicated.

Flight Research Center,
National Aeronautics and Space Administration,
Edwards, Calif., February 16, 1973.

REFERENCES

1. Thompson, Milton O.; Peterson, Bruce A.; and Gentry, Jerauld R.: Lifting-Body Flight Test Program. SETP Technical Review, second 1966 issue, vol. 8, no. 2, Sept. 1966, pp. 1-22.
2. Jenkins, Jerald M.; Tang, Ming H.; and Pearson, George P. E.: Vertical-Tail Loads and Control-Surface Hinge-Moment Measurements on the M2-F2 Lifting Body During Initial Subsonic Flight Tests. NASA TM X-1712, 1968.
3. Tang, Ming H.; and Pearson, George P. E.: Flight-Measured HL-10 Lifting Body Center Fin Loads and Control Surface Hinge Moments and Correlation With Wind-Tunnel Predictions. NASA TM X-2419, 1971.
4. Tang, Ming H.: Correlation of Flight-Test Loads With Wind-Tunnel Predicted Loads on Three Lifting Body Vehicles. Flight Test Results Pertaining to the Space Shuttlecraft. NASA TM X-2101, 1970, pp. 59-72.
5. Tang, Ming H.; and DeAngelis, V. Michael: Fin Loads and Control-Surface Hinge Moments Measured in Full-Scale Wind-Tunnel Tests on the X-24A Flight Vehicle. NASA TM X-1922, 1969.
6. Blake, W. W.: Transonic Test Results From a Force, Moment, and Control Surface Hinge Moment Investigation Conducted With an 8% Scale SV-5P Vehicle in the NASA-Langley 8-Foot Transonic Pressure Wind Tunnel. Eng. Rep. No. 13886, vols. I and II, Martin Co., Jan. 1966.
7. Stouffer, C. G.; and Hutton, B. L.: Transonic Pressure Test Results of an 8% Scale SV-5P Vehicle Tested at Cornell Aeronautical Laboratory, Inc., 8-Foot Wind Tunnel. Eng. Rep. No. 14113, vols. I and II, Martin Co., Mar. 1966.
8. Blake, W. W.; and Miller, M. C.: Supersonic Test Results From a Force, Moment, and Control Surface Hinge Moment Investigation Conducted With an 8-Percent Scale SV-5P Vehicle in the North American 7 x 7 Foot Trisonic Wind-Tunnel. Eng. Rep. No. 14079, vols. I and II, Martin Co., June 1966.
9. Mechty, E. A.: The International System of Units - Physical Constants and Conversion Factors. NASA SP-7012, 1969.
10. Richardson, Norman R.; and Pearson, Albin O.: Wind-Tunnel Calibrations of a Combined Pitot-Static Tube, Vane-Type Flow-Direction Transmitter, and Stagnation-Temperature Element at Mach Numbers From 0.60 to 2.87. NASA TN D-122, 1959.

TABLE 1. - REFERENCE AREAS AND DIMENSIONS OF THE FINS
AND CONTROL SURFACES ON THE X-24A FLIGHT VEHICLE

Center vertical fin (airfoil slab) -

Area, m ² (ft ²)	1.37 (14.7)
Mean aerodynamic chord, m (in.)	1.47 (57.9)
Root chord, m (in.)	1.88 (73.9)
Tip chord, m (in.)	0.96 (38.0)
Distance between root chord and mean aerodynamic chord, m (in.)	0.44 (17.3)
Span, m (in.)	0.99 (38.8)

Outboard vertical fin (airfoil cambered with leading-edge droop) -

Area, each, m ² (ft ²)	2.41 (25.9)
Mean aerodynamic chord, m (in.)	1.92 (75.7)
Root chord, m (in.)	2.58 (101.5)
Tip chord, m (in.)	1.05 (41.5)
Distance between root chord and mean aerodynamic chord, m (in.)	0.55 (21.6)
Span, m (in.)	1.27 (50.1)

Upper rudder -

Area, each, m ² (ft ²)	0.46 (4.99)
Chord, m (in.)	0.75 (29.6)
Span, m (in.)	0.62 (24.2)

Lower rudder -

Area, each, m ² (ft ²)	0.62 (6.67)
Chord, m (in.)	0.75 (29.6)
Span, m (in.)	0.82 (32.4)

Upper flap -

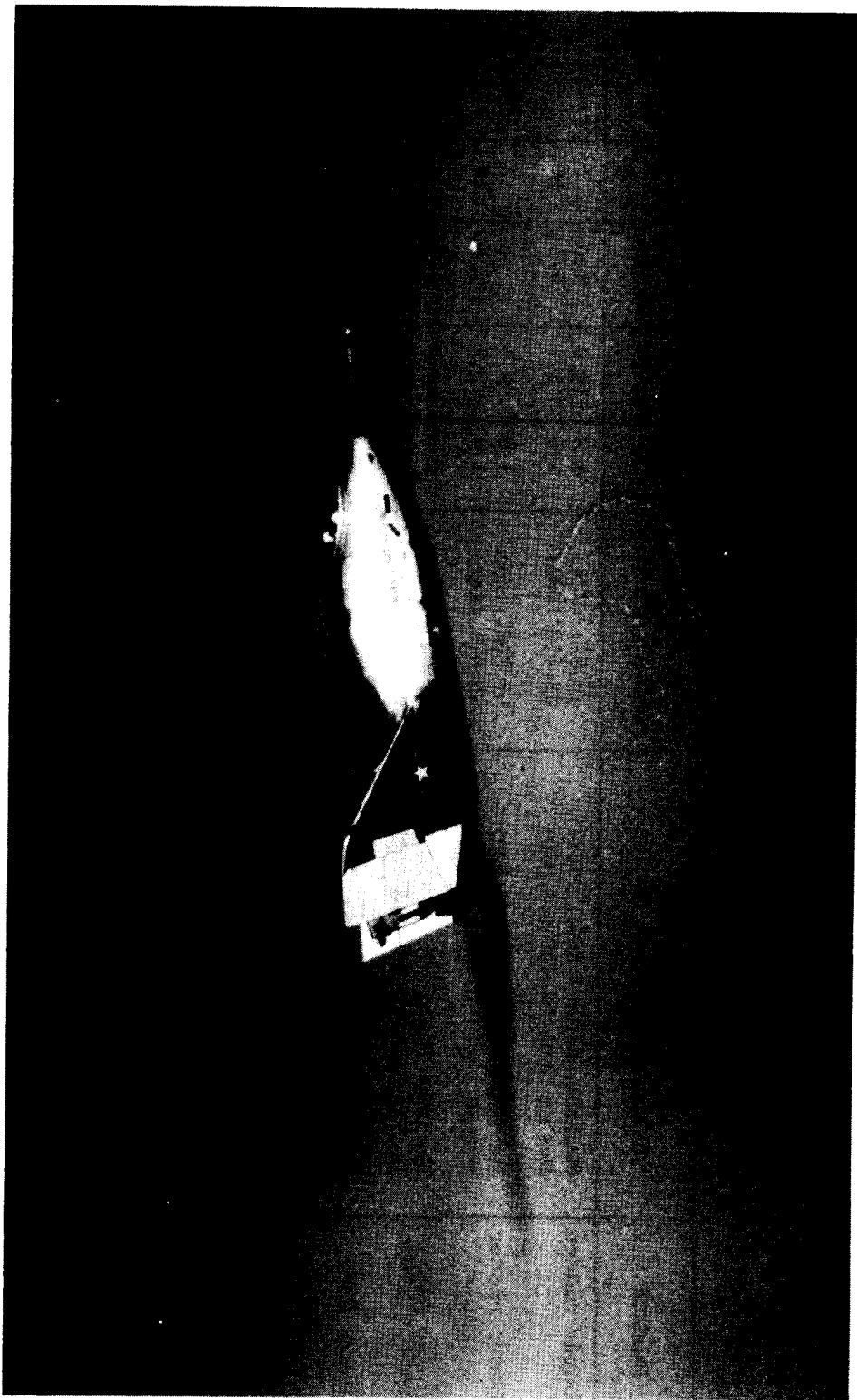
Area, each, m ² (ft ²)	1.01 (10.82)
Chord, m (in.)	0.87 (34.1)
Span, m (in.)	1.16 (45.7)

Lower flap -

Area, each, m ² (ft ²)	1.30 (13.99)
Chord, m (in.)	1.14 (44.9)
Span, m (in.)	1.14 (44.9)

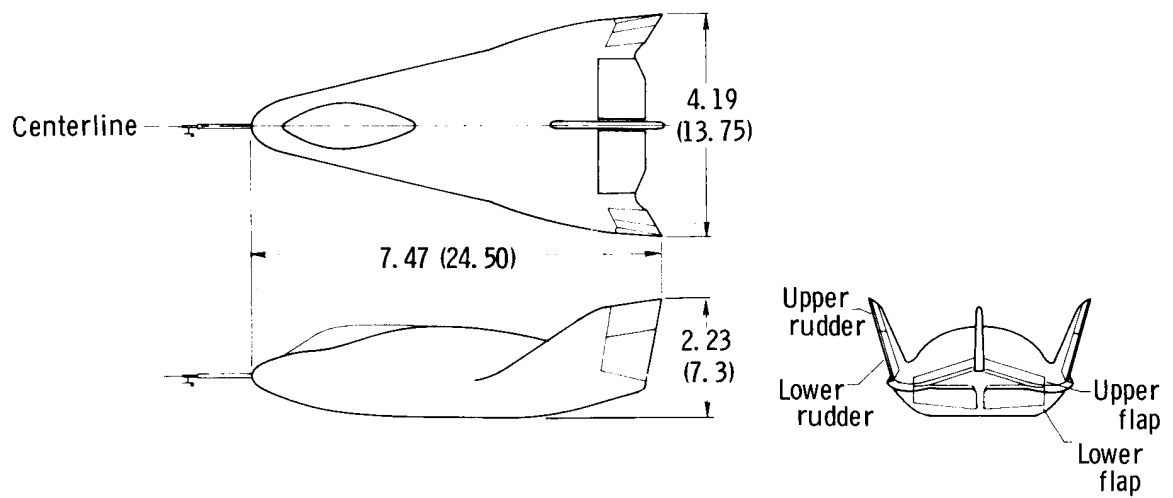
TABLE 2.- MAXIMUM X-24A FLIGHT AND DESIGN-LIMIT CONTROL-SURFACE HINGE
MOMENTS AND ASSOCIATED CONDITIONS

Surface	Hinge moment, m-N (in-lb)	q , N/m ² (lb/ft ²)	M	α , deg	β , deg	δ_{rb} , deg	δ_u , deg	δ_l , deg
Upper rudder	Maximum flight = 836 (7,400) Design limit = 2,700 (23,900)	10,821 (226) 23,078 (482)	0.8 1.6	14.6 5.7	-1.0 -5.5	2 10	-40 --	23 --
Lower rudder	Maximum flight = 508 (4,500) Design limit = 3,434 (30,400)	7,948 (166) 23,078 (482)	1.6 1.6	6.7 5.7	0 -5.5	2 10	-40 --	19 --
Upper flap	Maximum flight = 3,412 (30,200) Design limit = 8,868 (78,500)	9,049 (189) 23,030 (481)	0.9 1.7	10.0 4.0	0 0	0 --	-40 -54	29 --
Lower flap	Maximum flight = 3,604 (31,900) Design limit = 10,168 (90,000)	9,863 (206) 22,312 (466)	0.9 1.4	15.1 12.0	0 0	0 --	-40 --	26 40



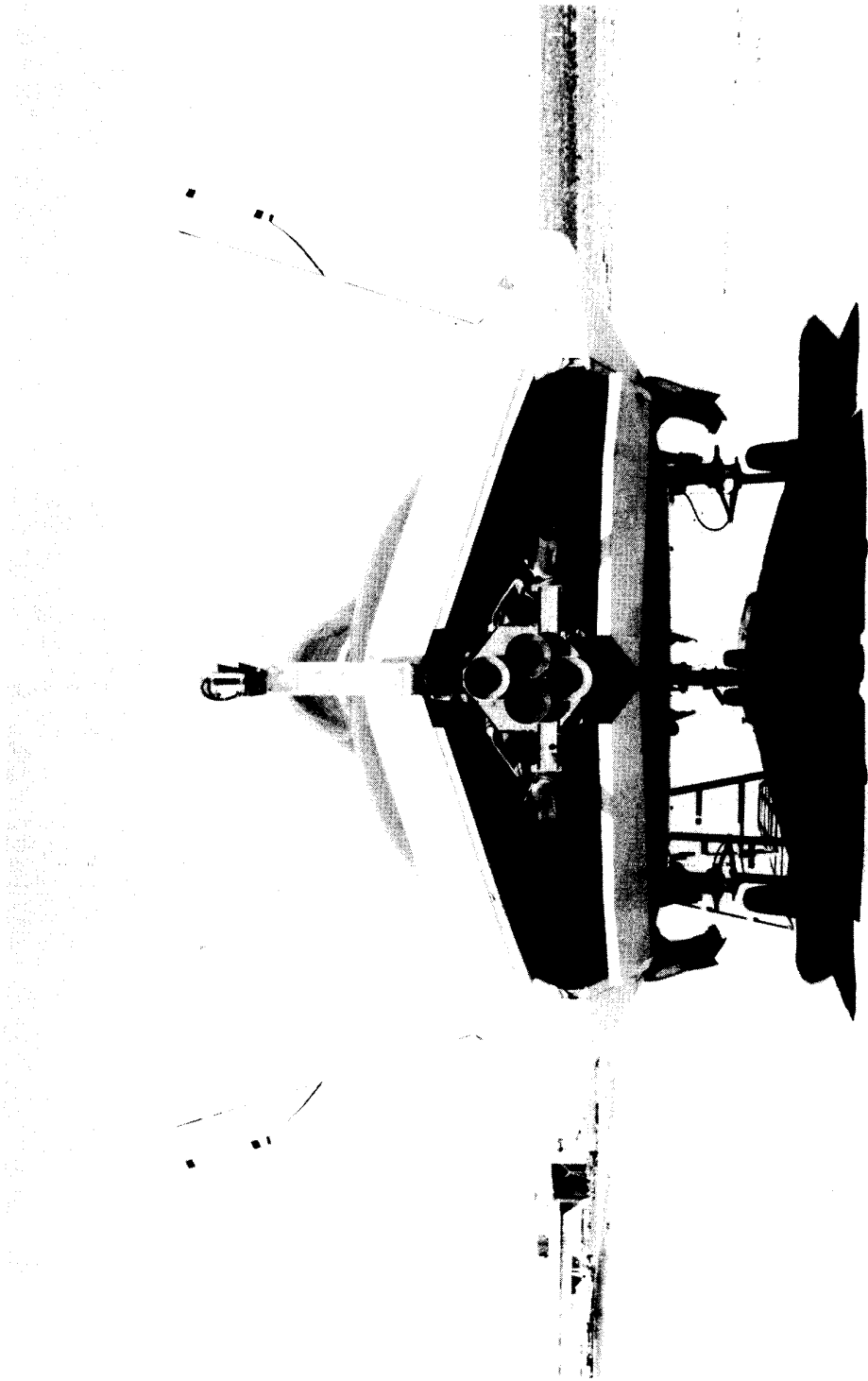
(a) Flight-test vehicle.

Figure 1. X-24A lifting body vehicle.



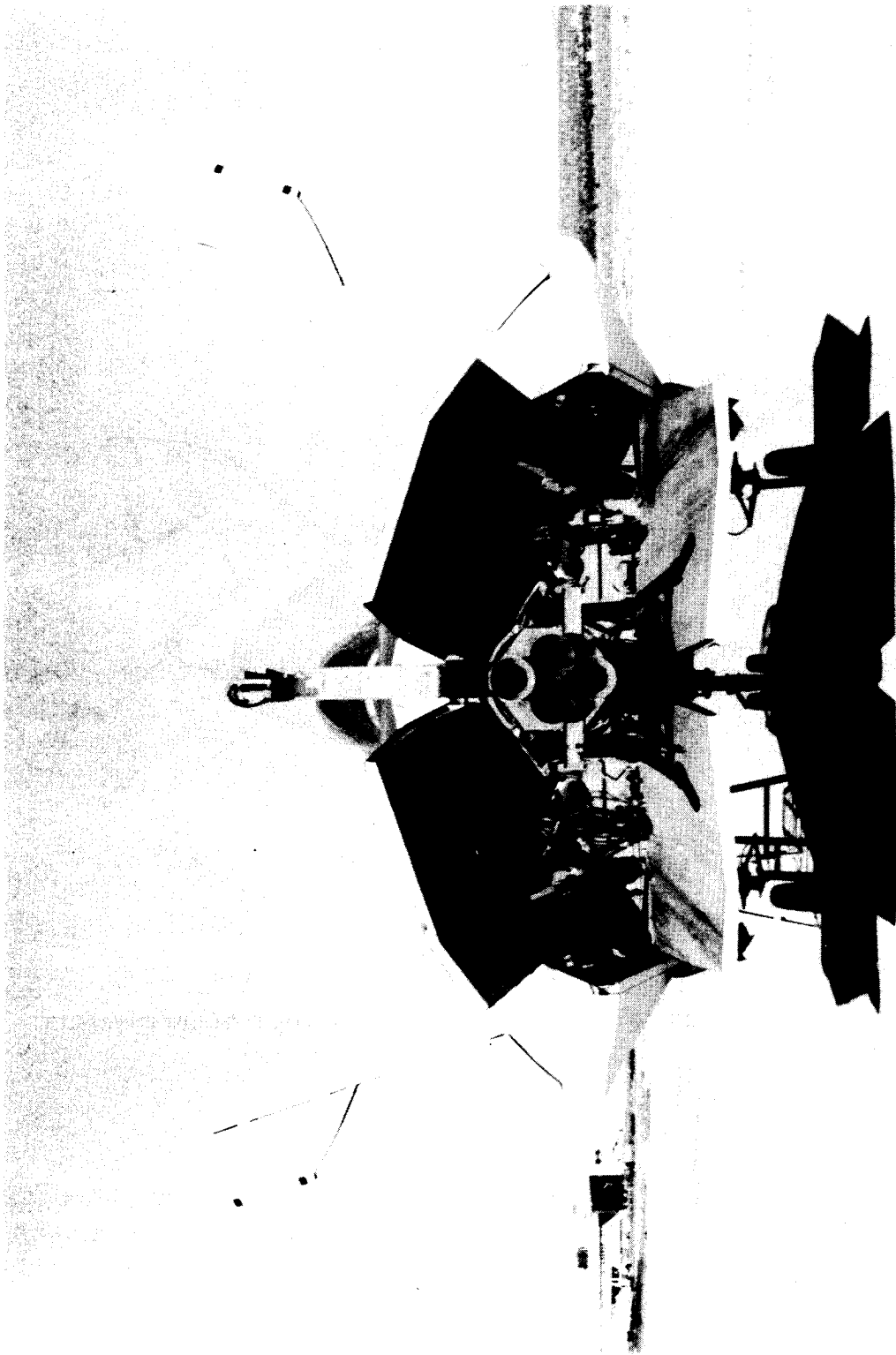
(b) Three-view drawing. Dimensions in meters (feet).

Figure 1. Concluded.



(a) $\delta_u = -13^\circ$, $\delta_l = 10^\circ$, and $\delta_{rb} = -10^\circ$. E-23387

Figure 2. Rear view of X-24A lifting body vehicle.



(b) $\delta_u = -40^\circ$, $\delta_l = 25^\circ$, and $\delta_{rb} = 0^\circ$. E-23391

Figure 2. Concluded.

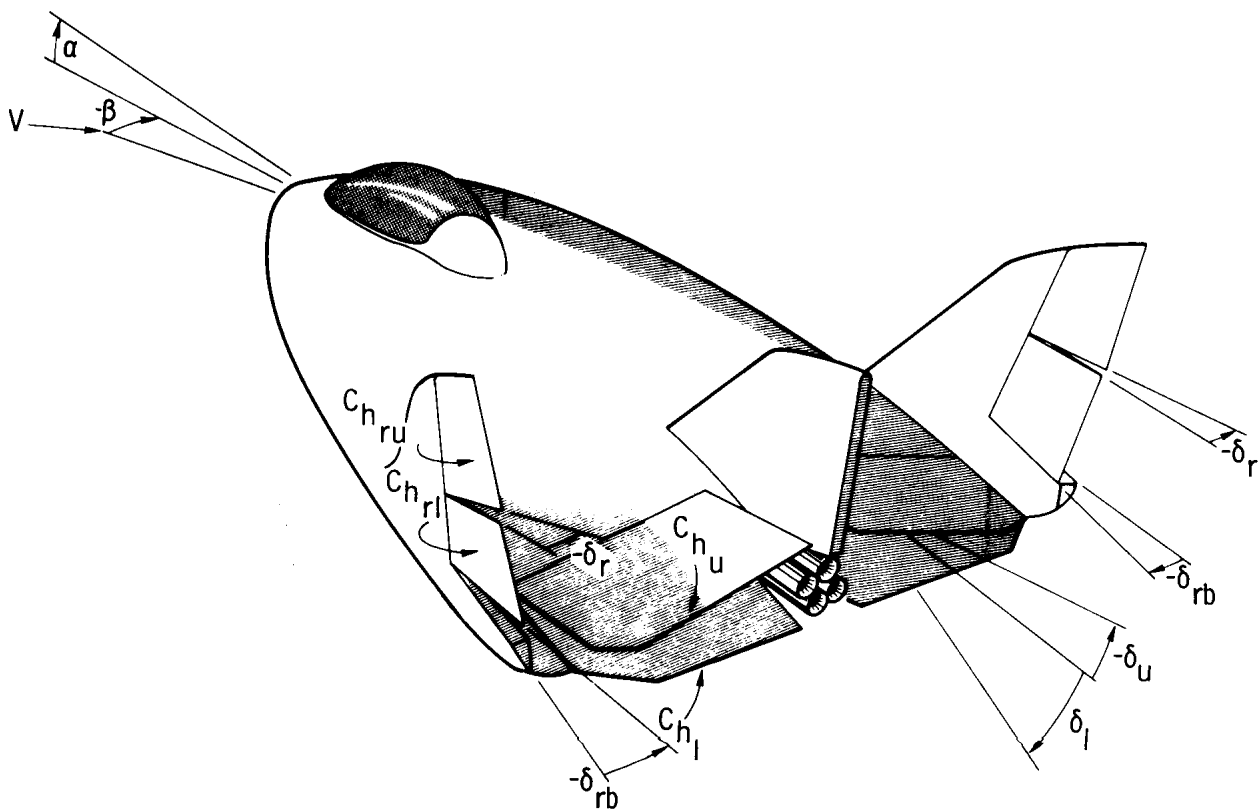
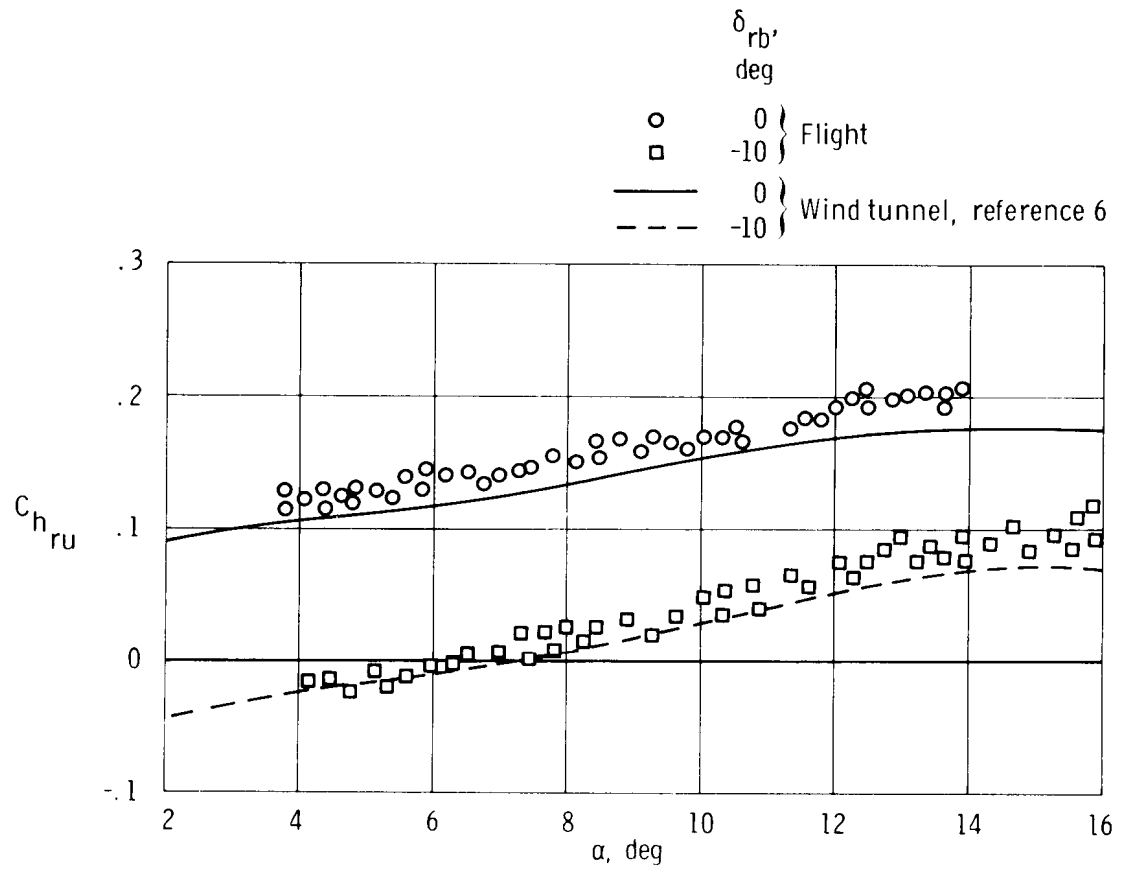
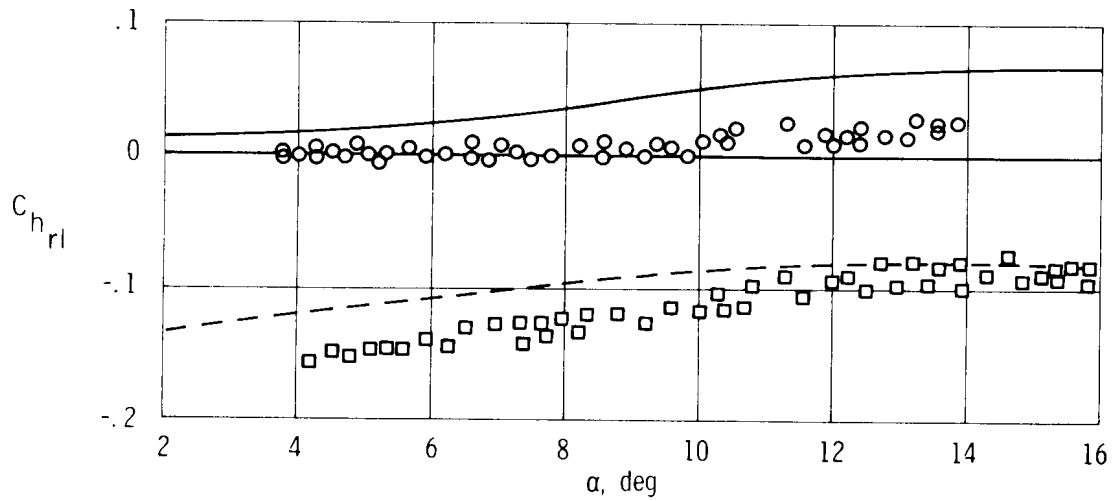


Figure 3. Sign convention for the X-24A control-surface hinge moments and deflections.

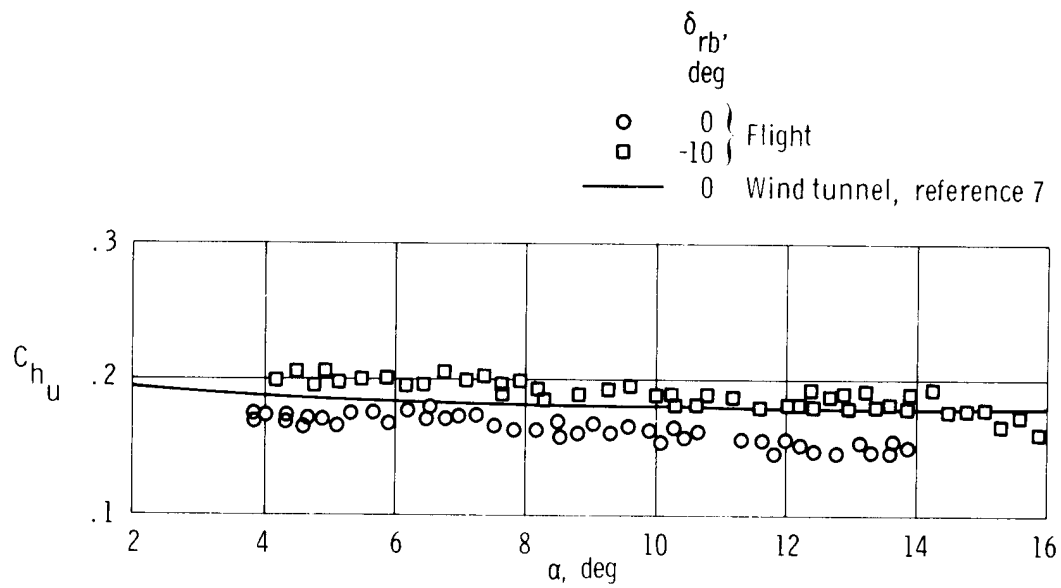


(a) Upper rudder.

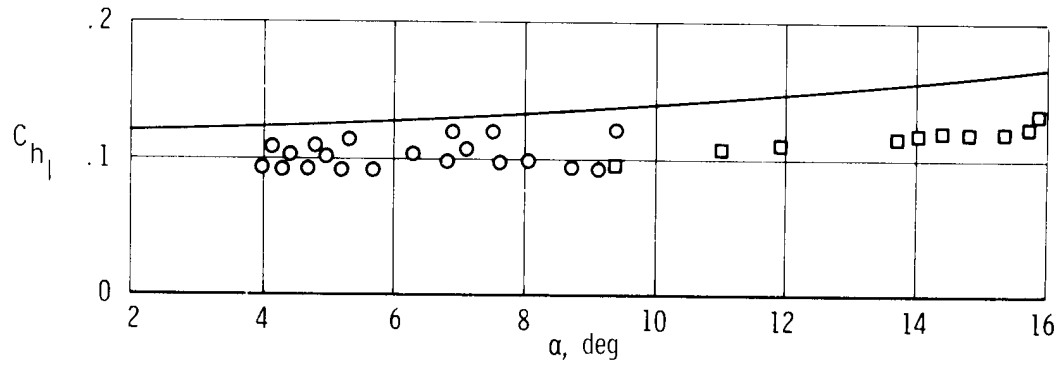


(b) Lower rudder.

Figure 4. Variation of control-surface hinge-moment coefficients with angle of attack and rudder bias. $M = 0.6$; $\beta = 0^\circ$; $\delta_r = 0^\circ$; $\delta_u = -30^\circ$; $\delta_l = 20^\circ$.

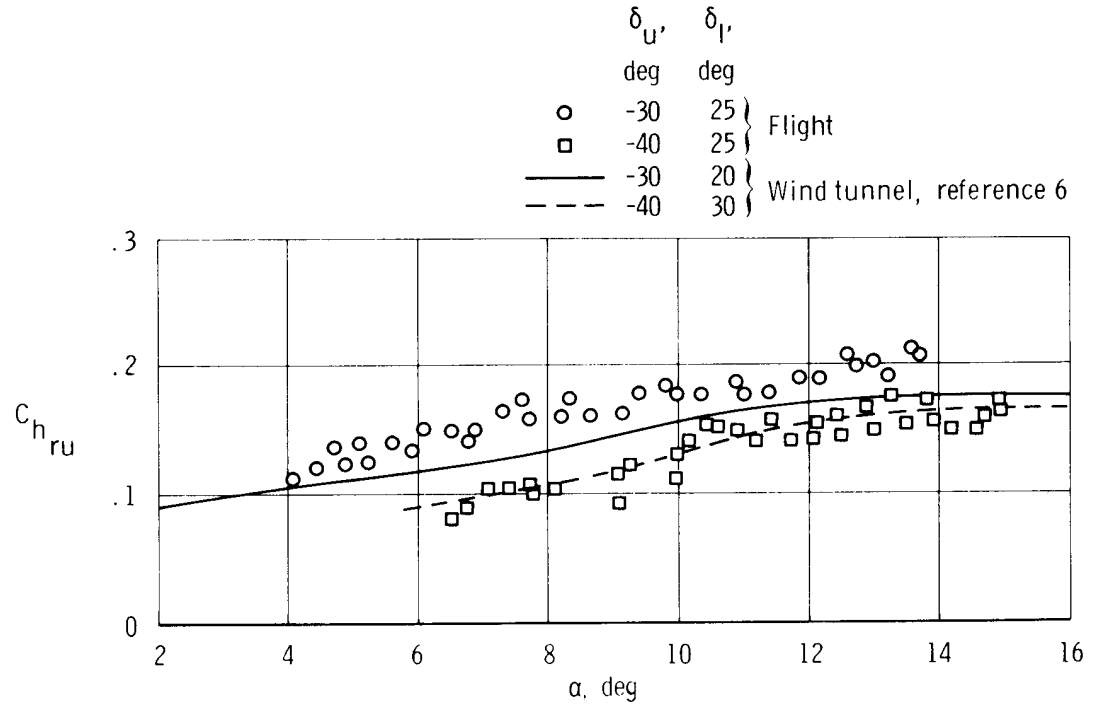


(c) Upper flap.

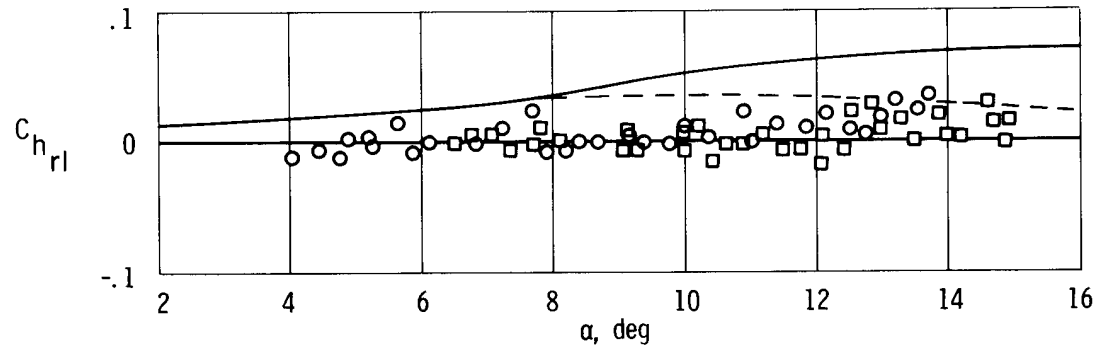


(d) Lower flap.

Figure 4. Concluded.

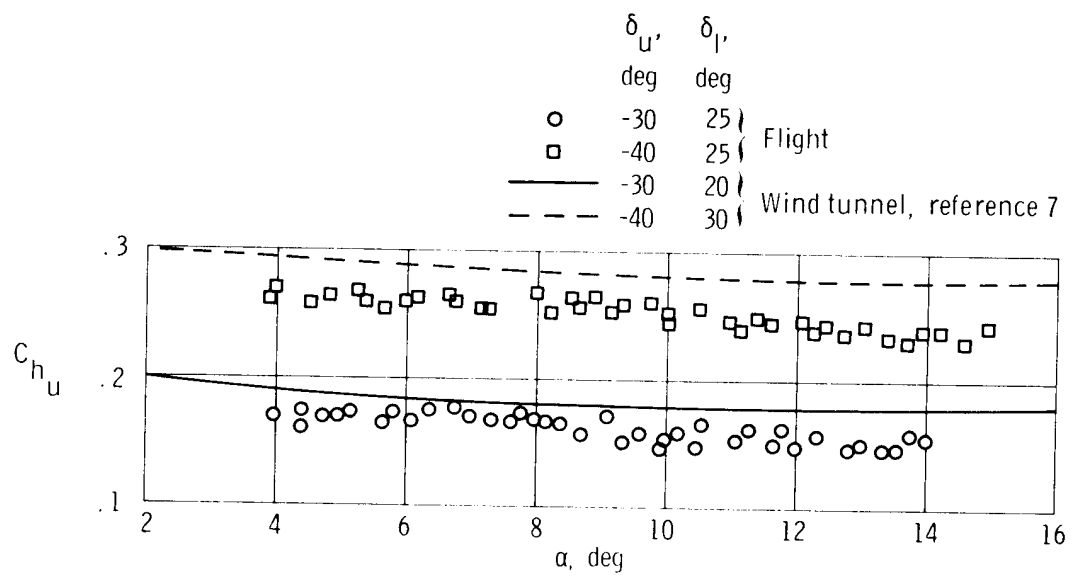


(a) Upper rudder.

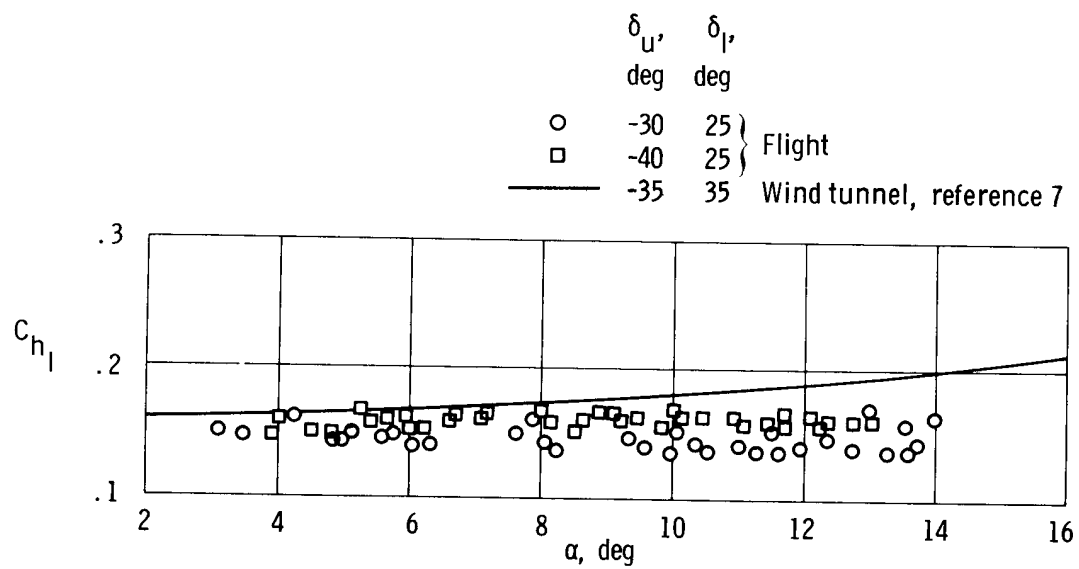


(b) Lower rudder.

Figure 5. Variation of control-surface hinge-moment coefficients with angle of attack and upper-flap deflection. $M = 0.6$; $\beta = 0^\circ$; $\delta_{rb} = 0^\circ$; $\delta_r = 0^\circ$.

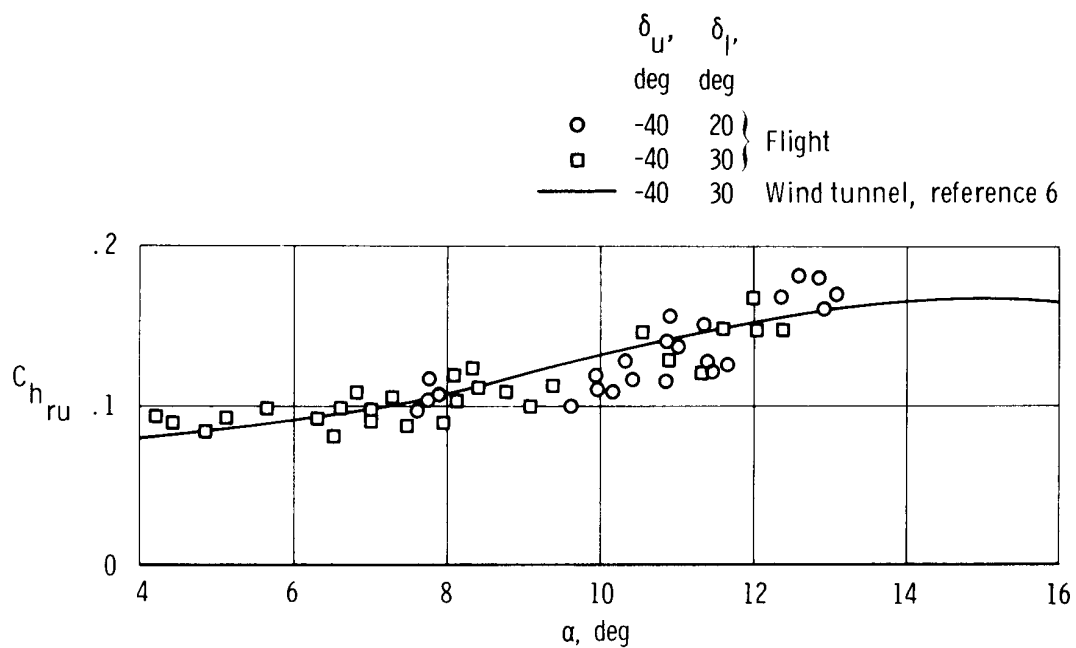


(c) Upper flap.

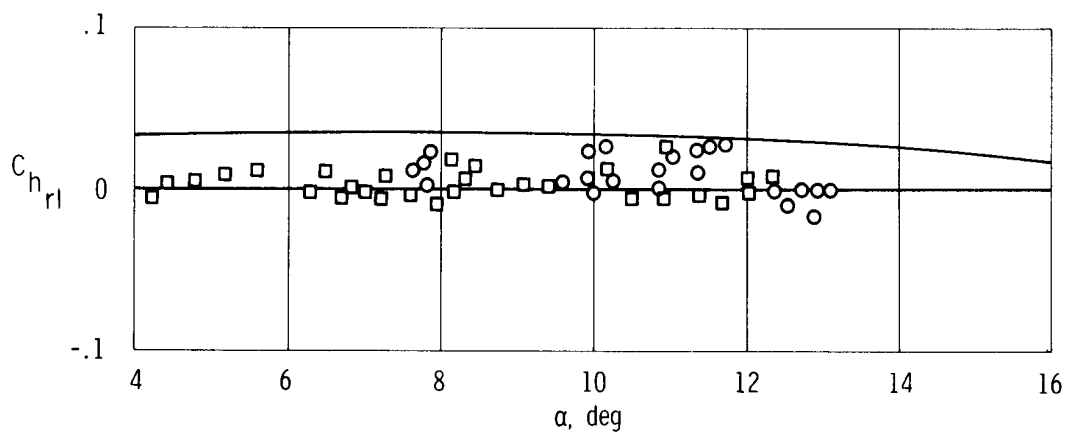


(d) Lower flap.

Figure 5. Concluded.

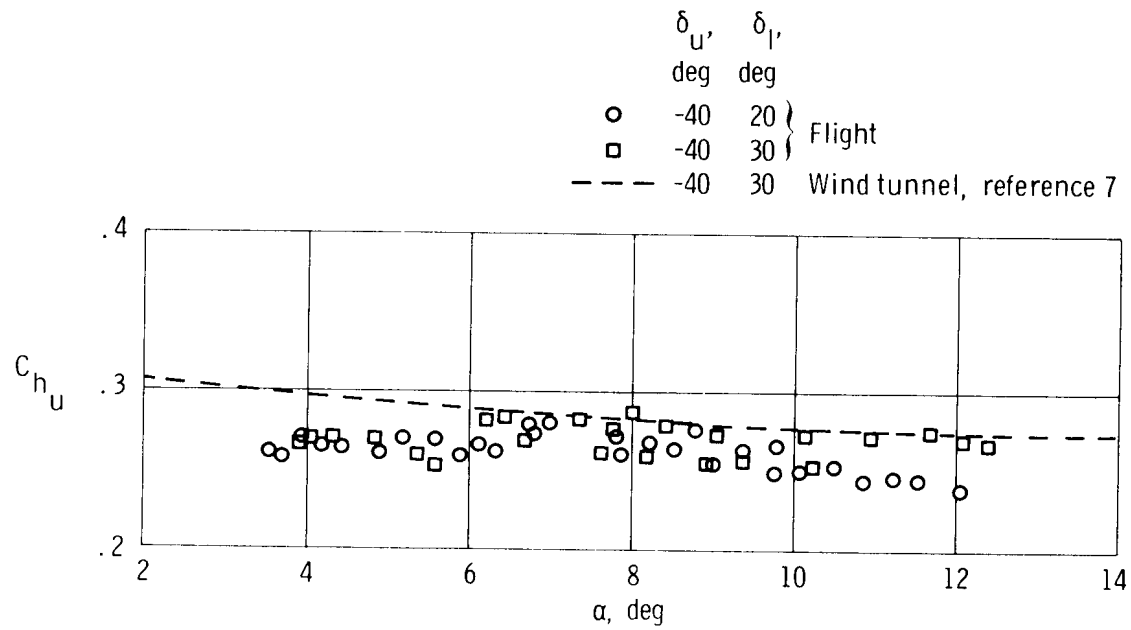


(a) Upper rudder.

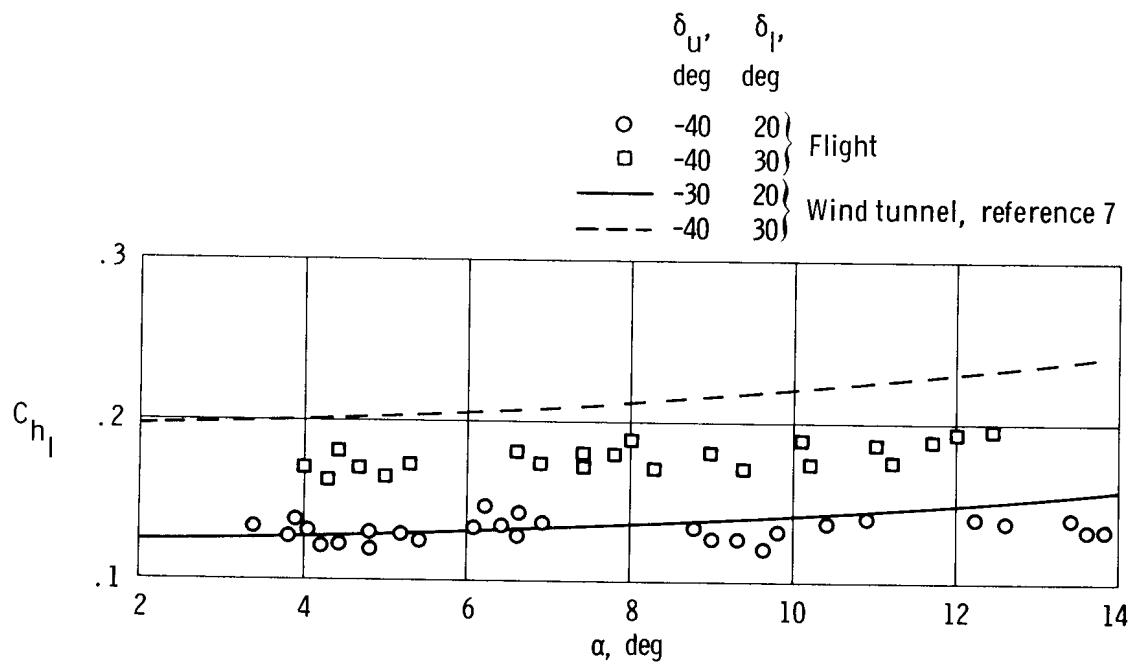


(b) Lower rudder.

Figure 6. Variation of control-surface hinge-moment coefficients with angle of attack and lower-flap deflection. $M = 0.6$; $\beta = 0^\circ$; $\delta_{rb} = 0^\circ$; $\delta_r = 0^\circ$.

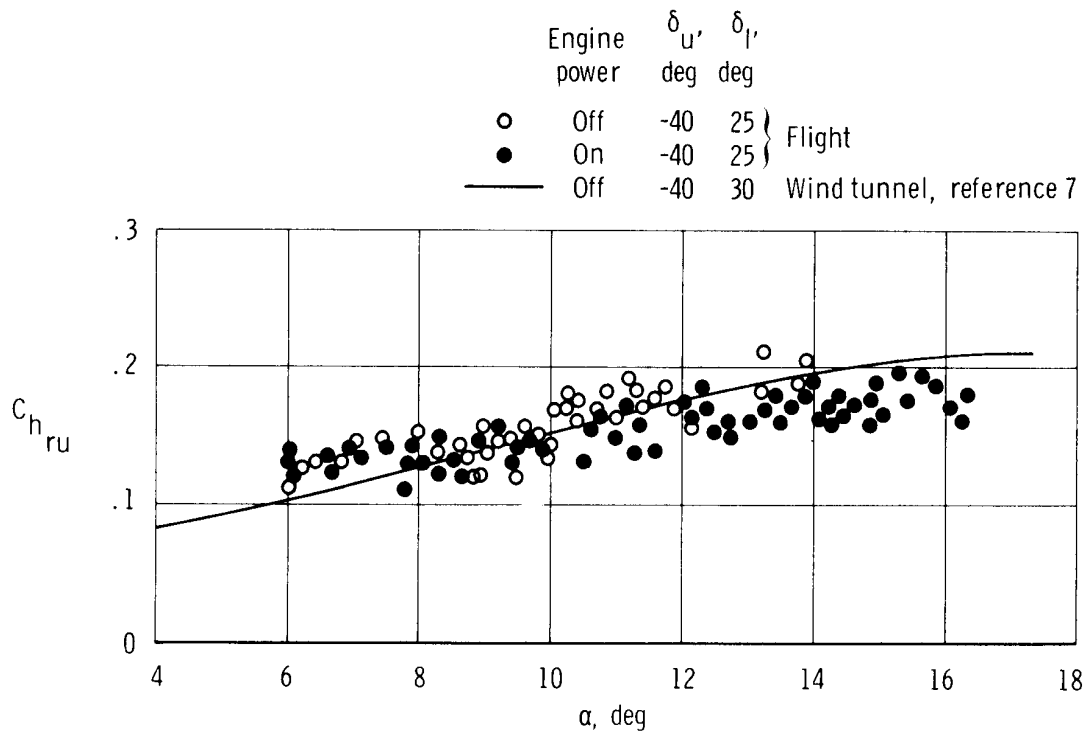


(c) Upper flap.

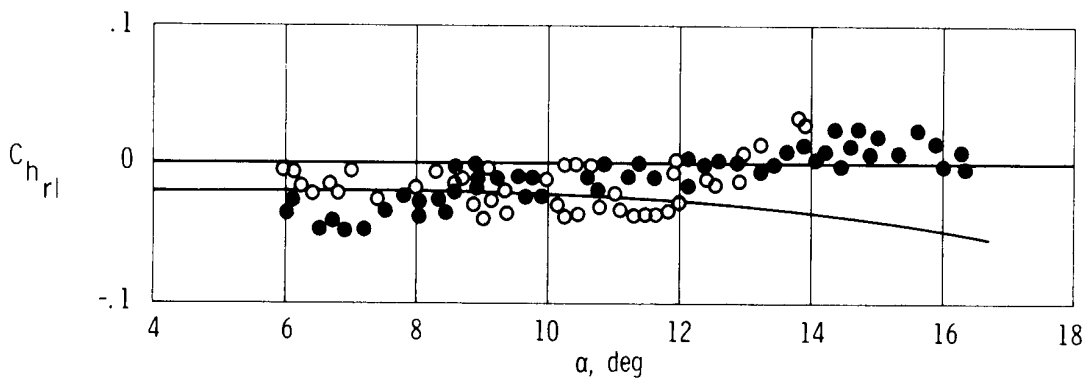


(d) Lower flap.

Figure 6. Concluded.

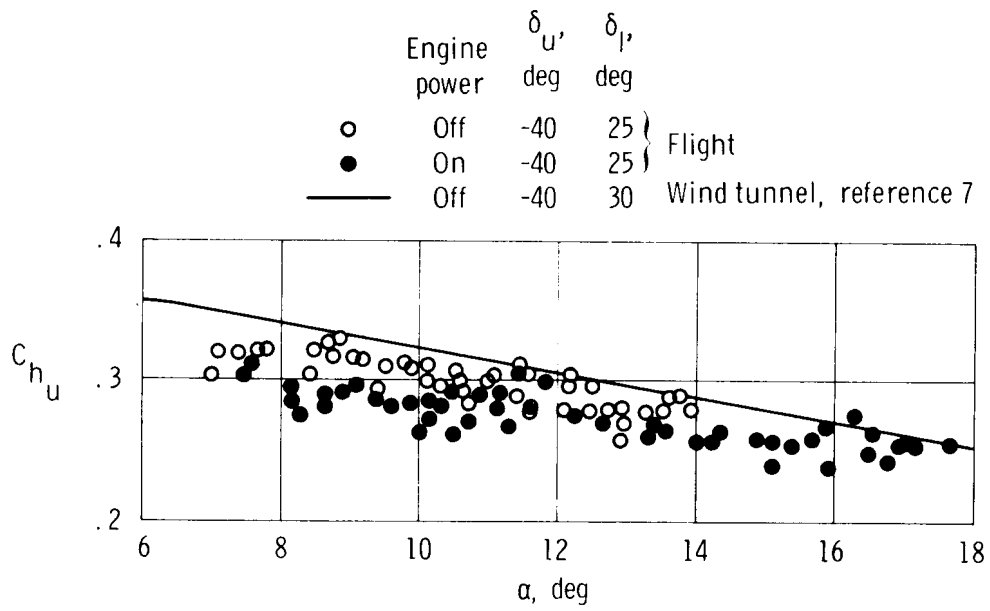


(a) Upper rudder.

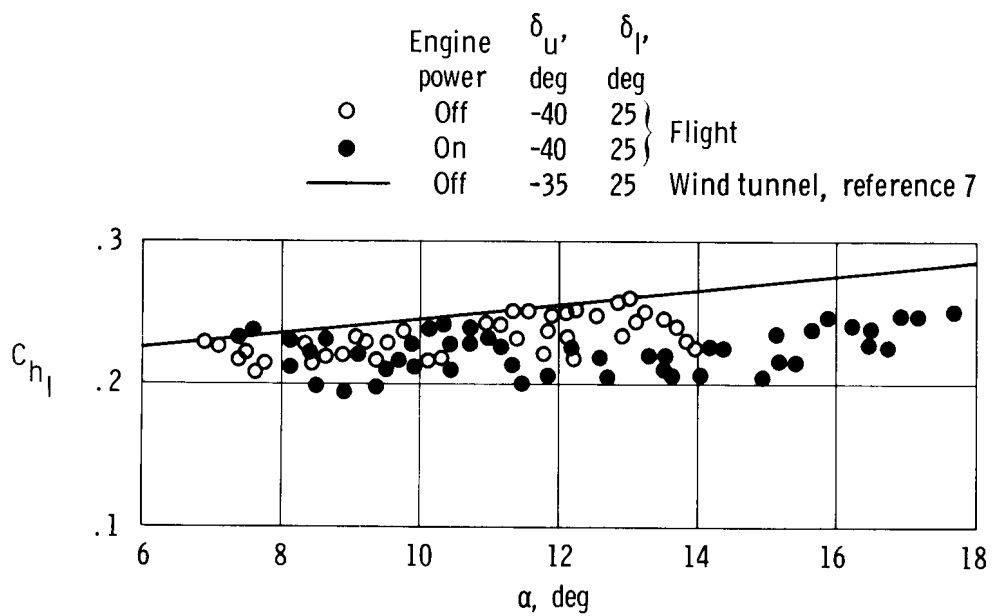


(b) Lower rudder.

Figure 7. Effect of rocket-engine operation on the variation of control-surface hinge-moment coefficients with angle of attack. $M = 0.9$; $\beta = 0^\circ$; $\delta_r = 0^\circ$; $\delta_{rb} = 0^\circ$.

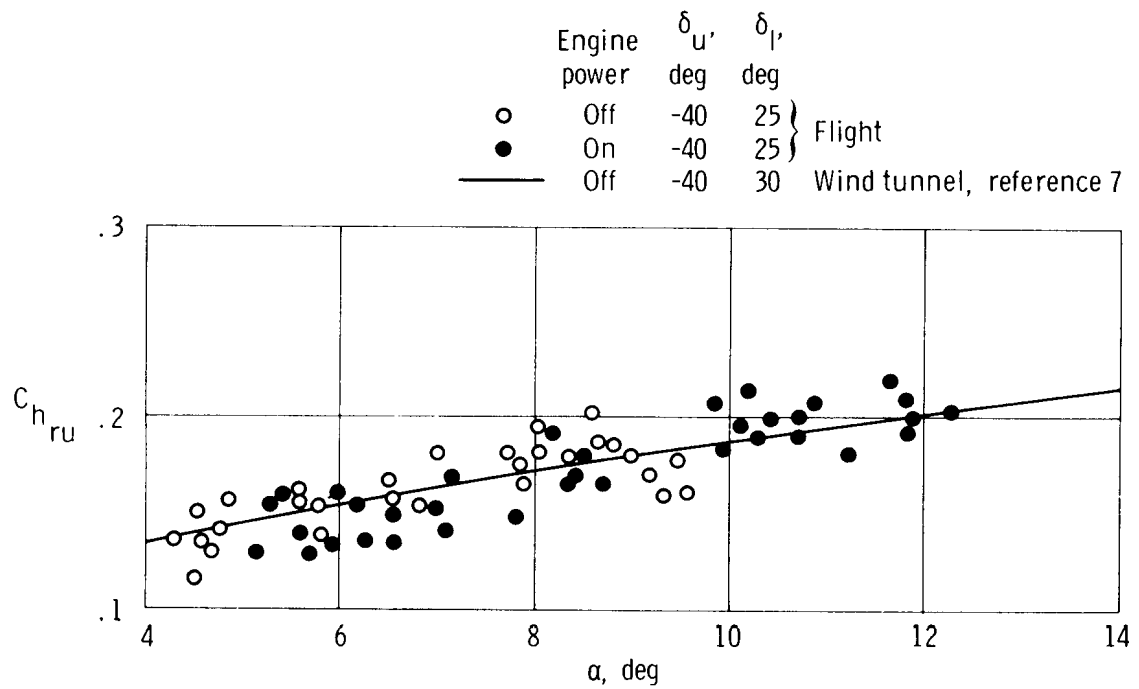


(c) Upper flap.

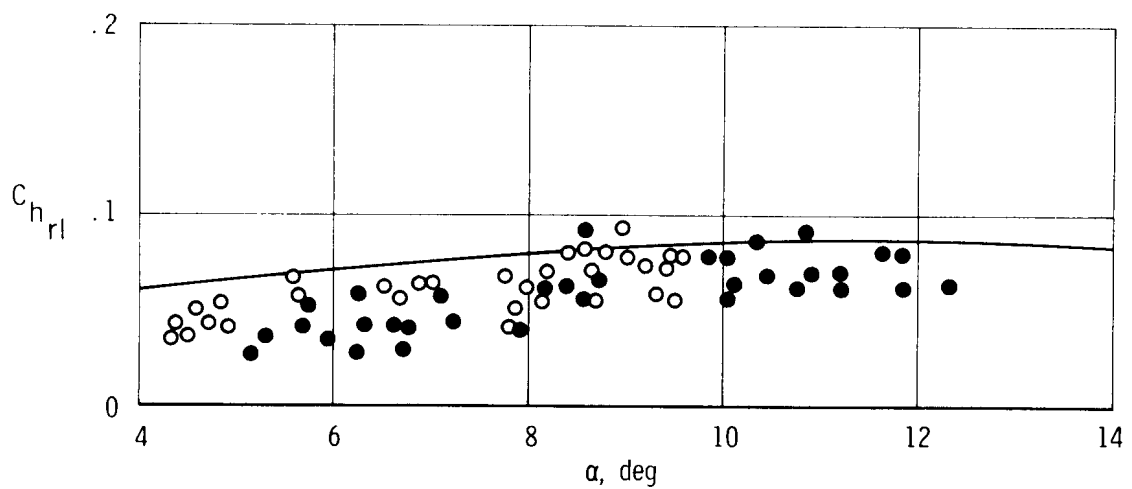


(d) Lower flap.

Figure 7. Concluded.

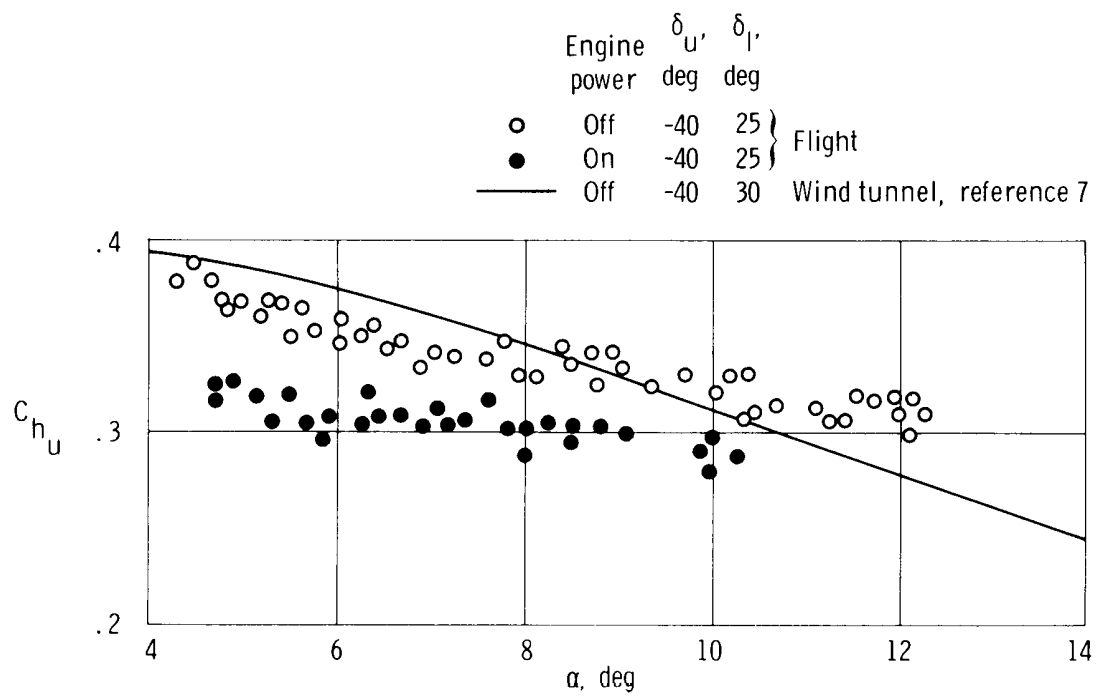


(a) Upper rudder.



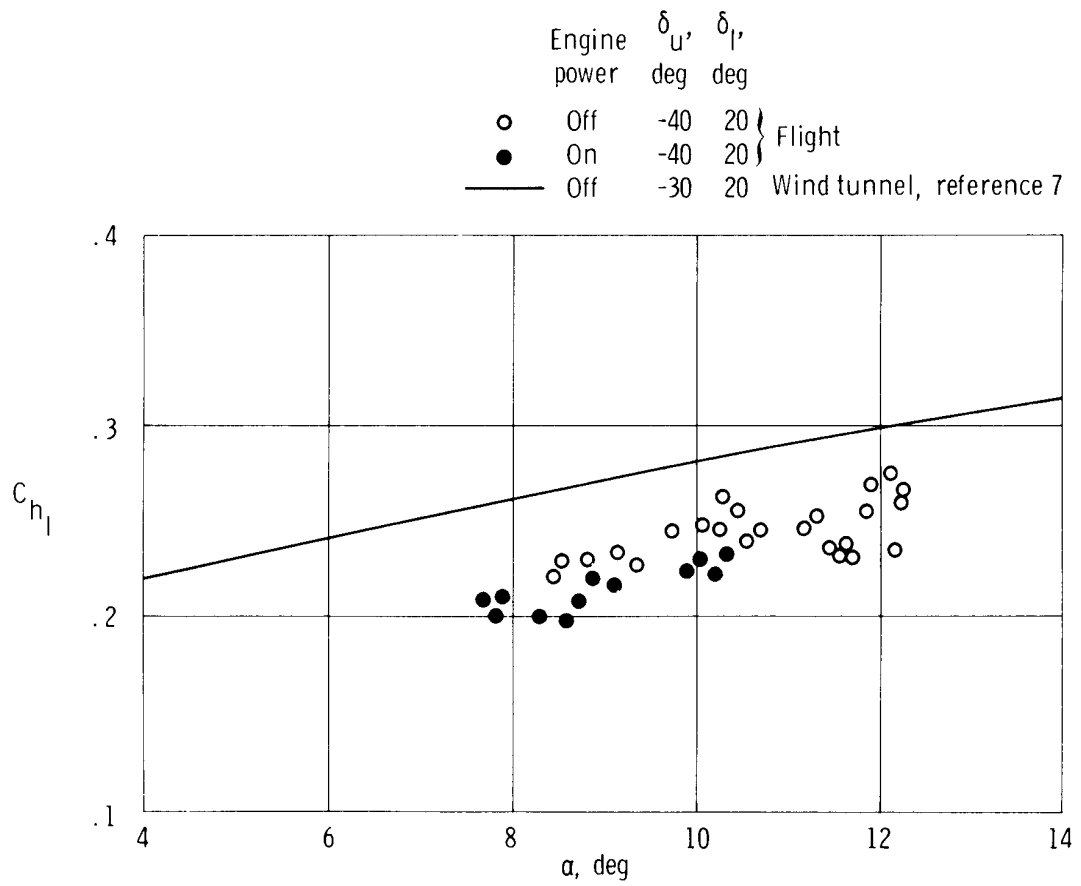
(b) Lower rudder.

Figure 8. Effect of rocket-engine operation on the variation of control-surface hinge-moment coefficients with angle of attack. $M = 1.2$; $\beta = 0^\circ$; $\delta_r = 0^\circ$; $\delta_{rb} = 0^\circ$.



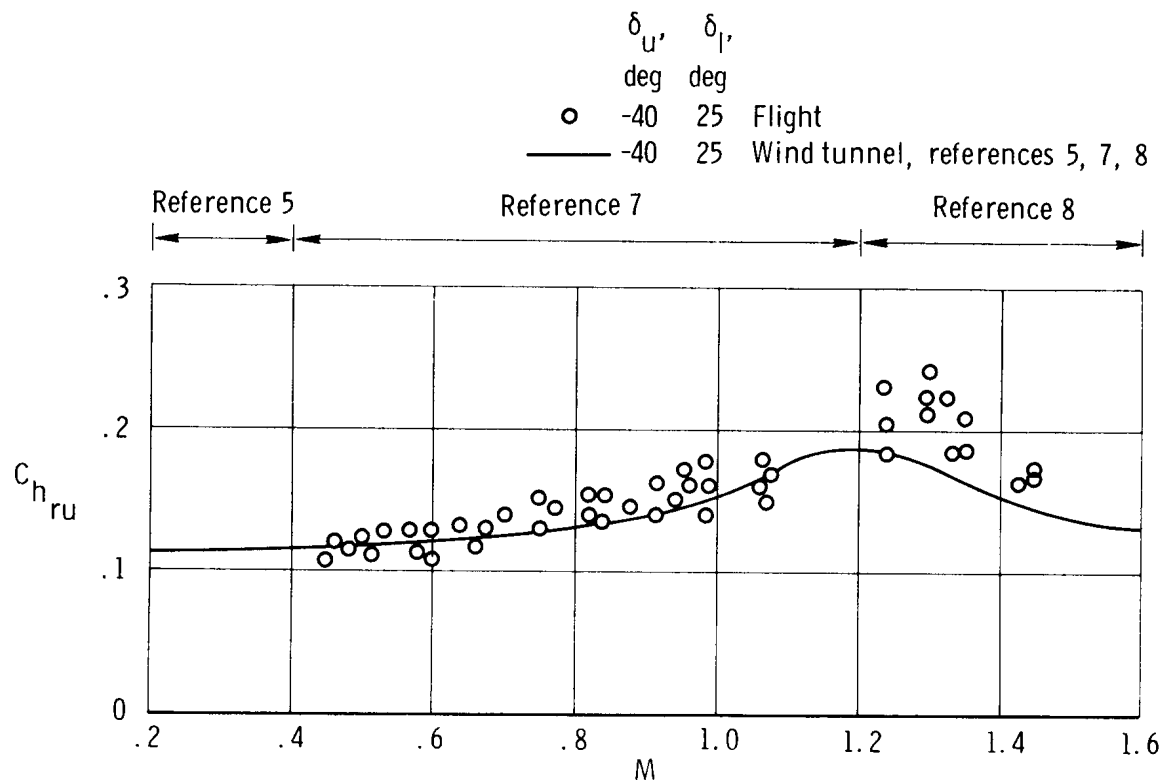
(c) Upper flap.

Figure 8. Continued.

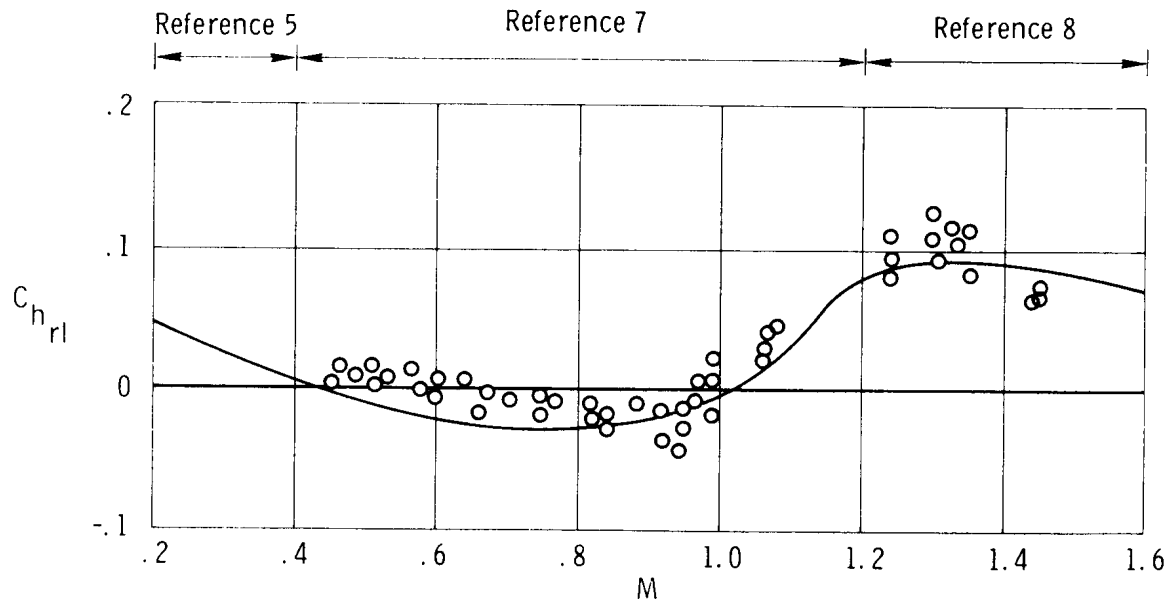


(d) Lower flap .

Figure 8. Concluded .

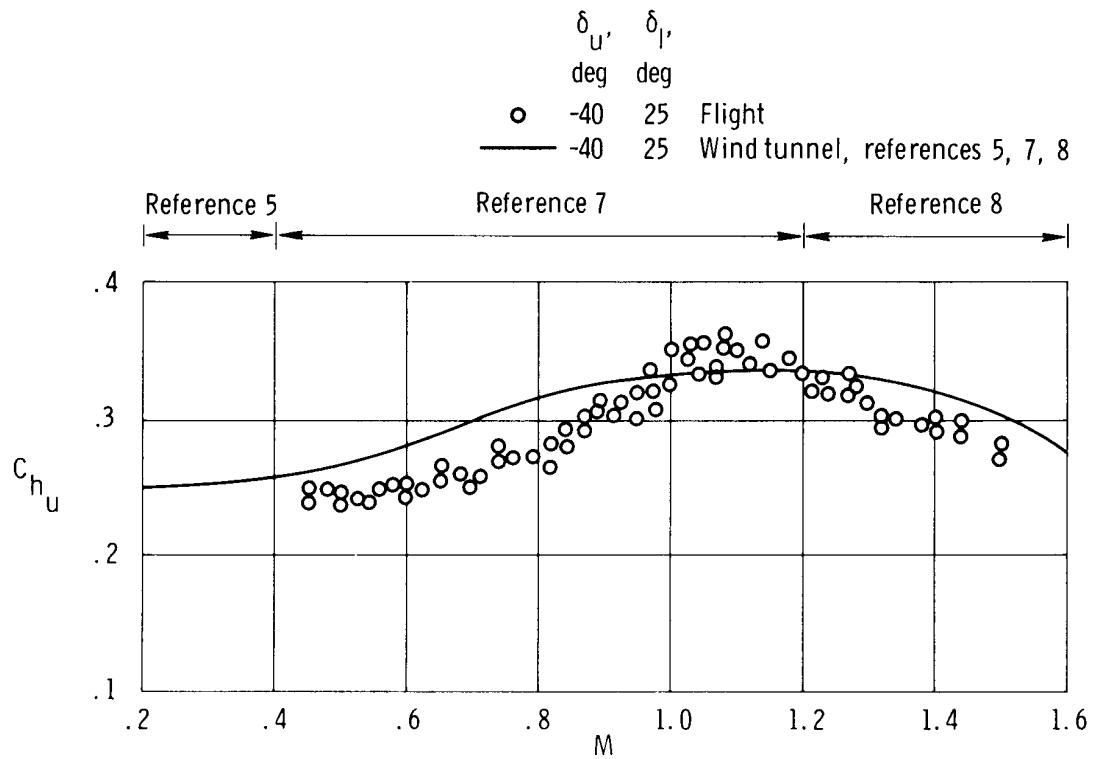


(a) Upper rudder.

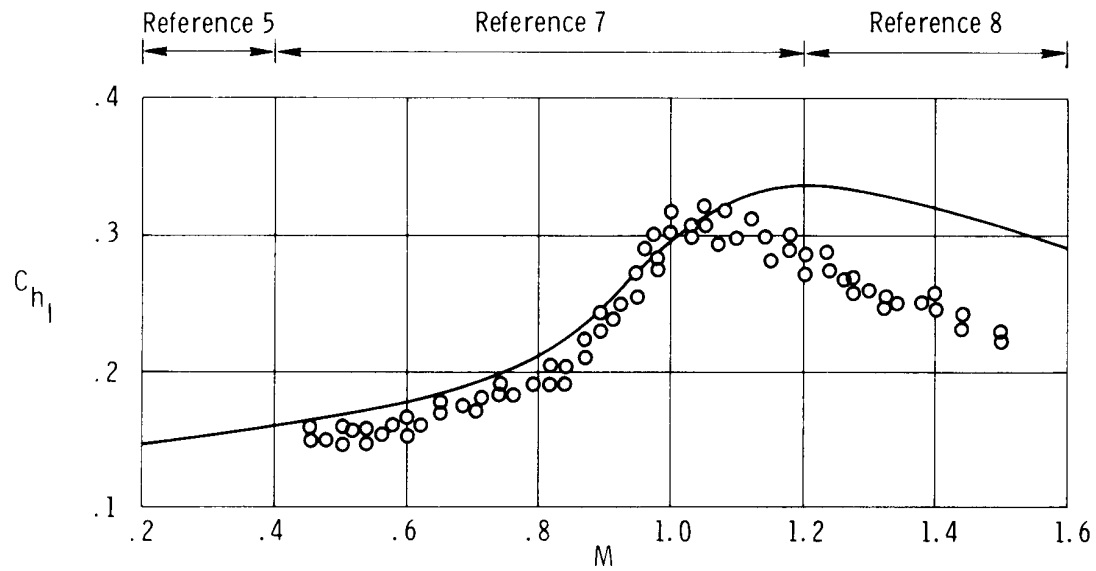


(b) Lower rudder.

Figure 9. Variation of control-surface hinge-moment coefficients with Mach number. $\alpha = 10^\circ$; $\beta = 0^\circ$; $\delta_r = 0^\circ$; $\delta_{rb} = 0^\circ$.

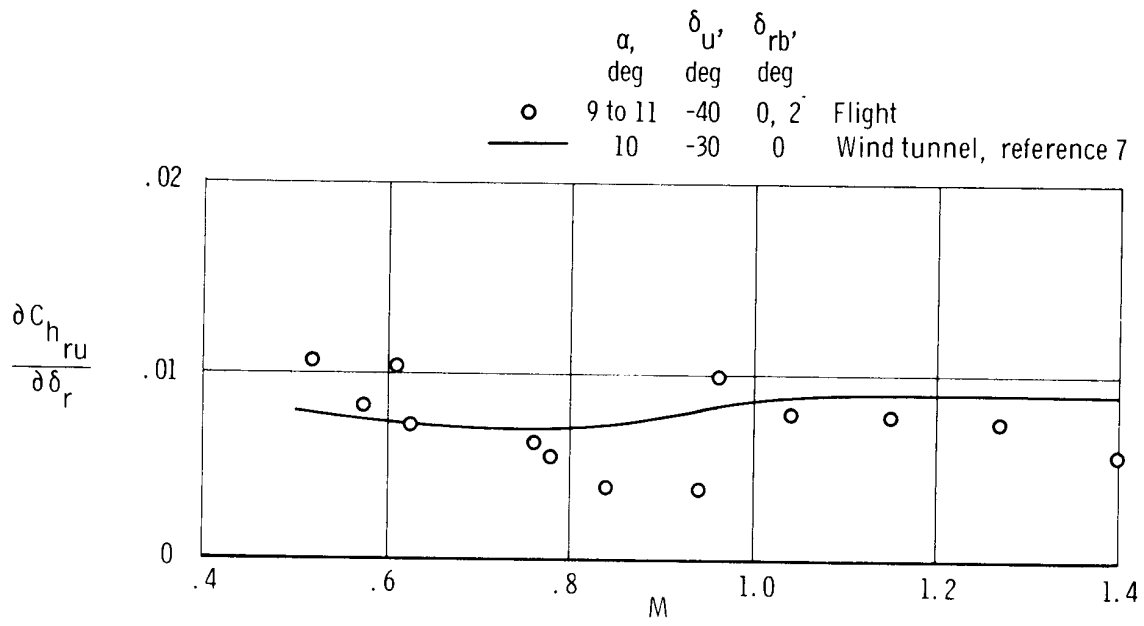


(c) Upper flap.

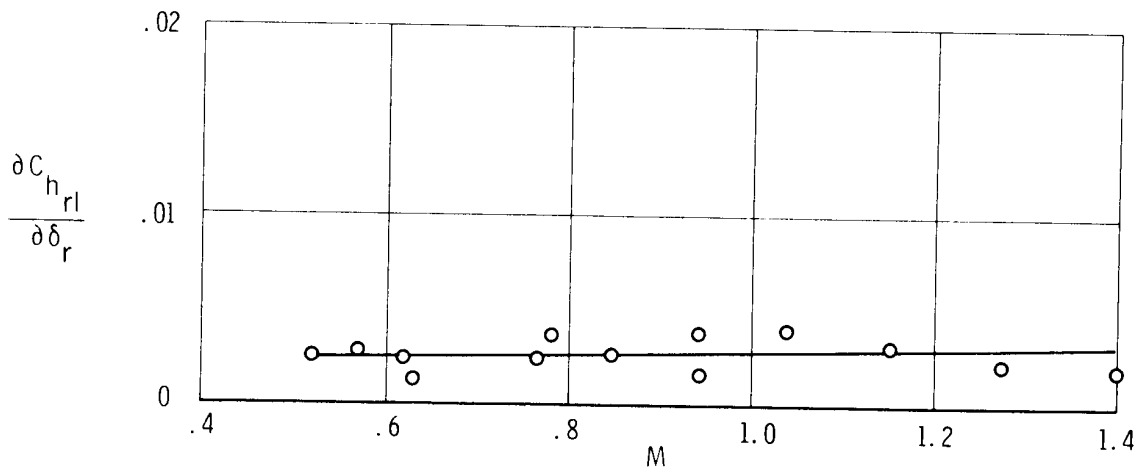


(d) Lower flap.

Figure 9. Concluded.

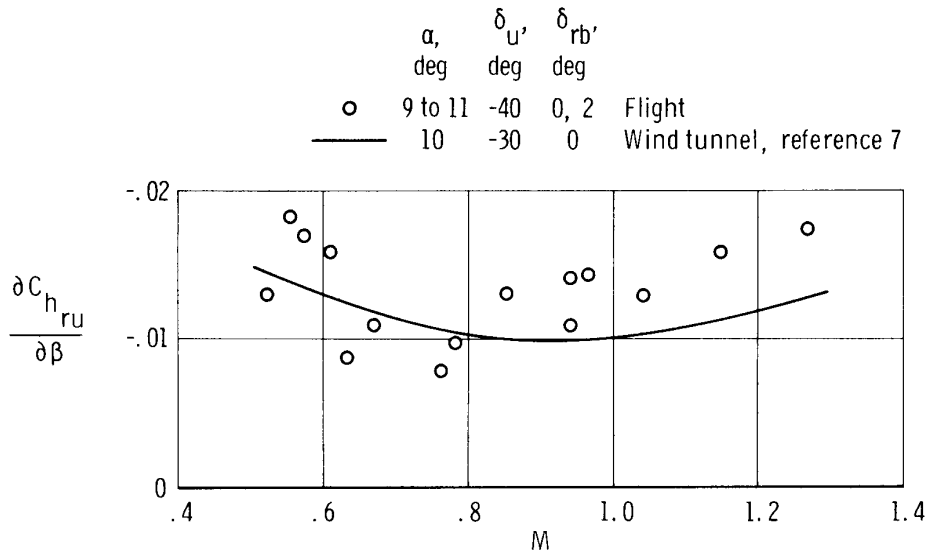


(a) Upper rudder.

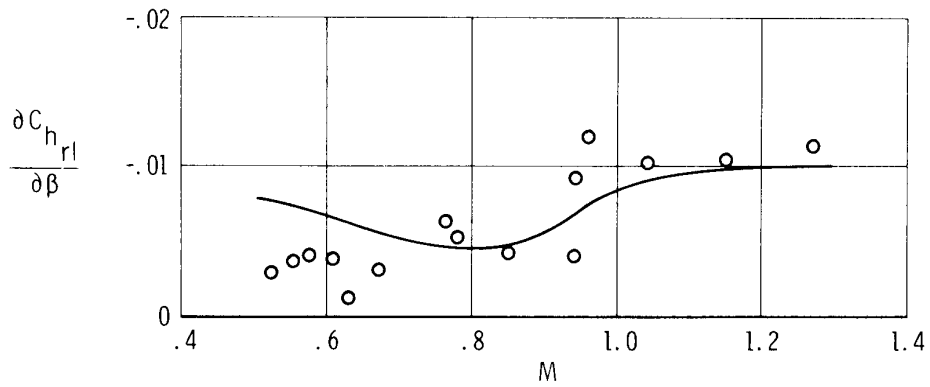


(b) Lower rudder.

Figure 10. Variation of the upper- and lower-rudder hinge-moment coefficients due to rudder deflection as a function of Mach number.

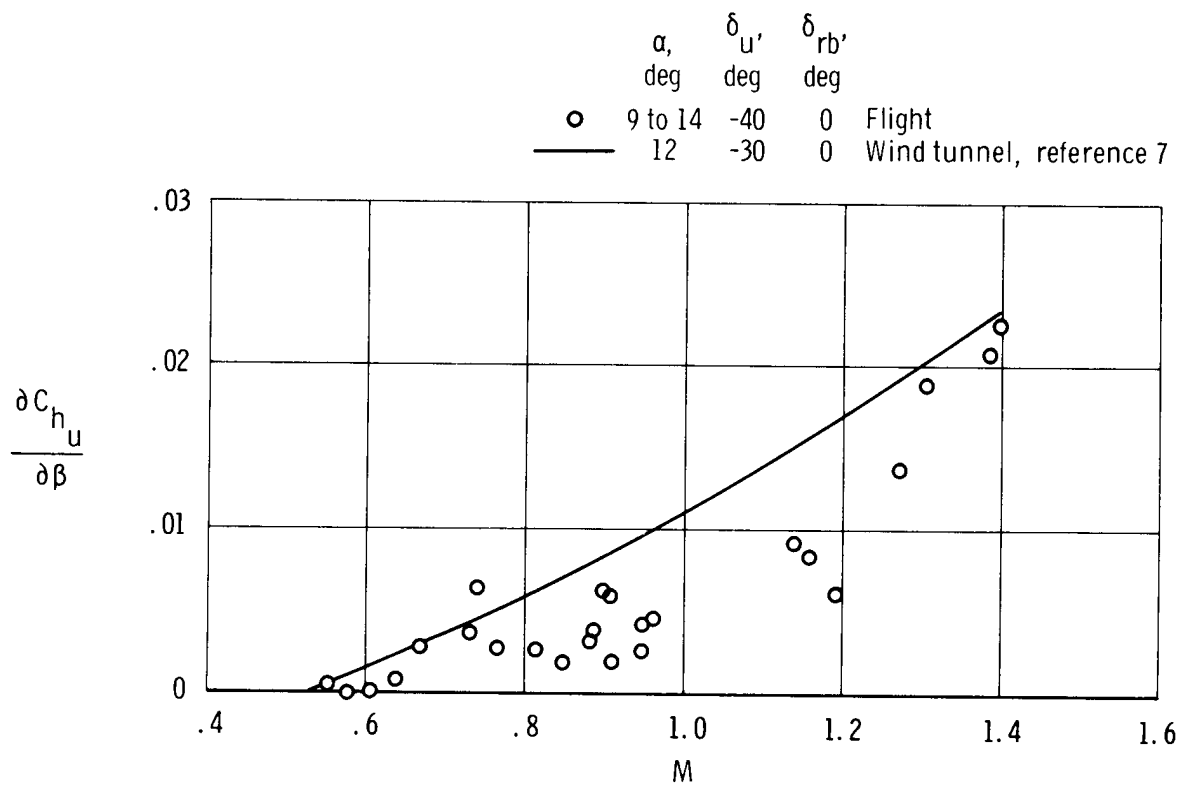


(a) Upper rudder.



(b) Lower rudder.

Figure 11. Variation of the upper- and lower-rudder and upper-flap hinge-moment coefficients due to angle of sideslip as a function of Mach number.



(c) Upper flap.

Figure 11. Concluded.

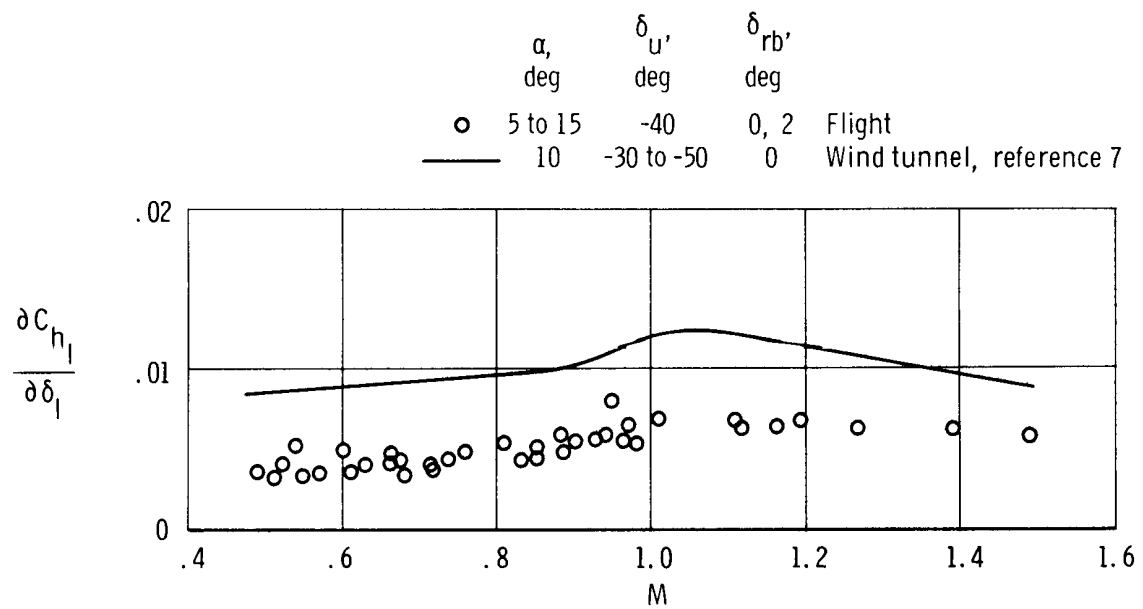
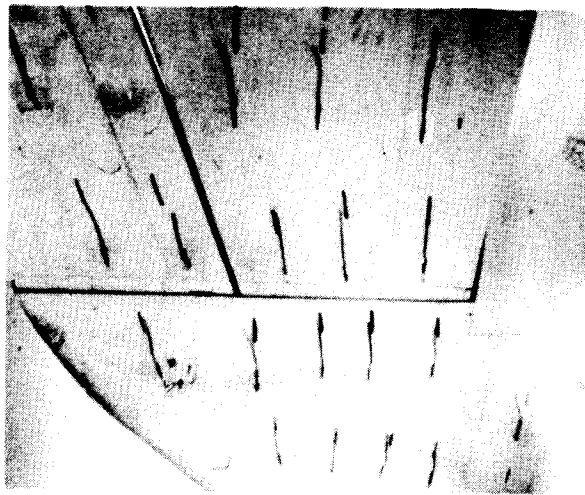
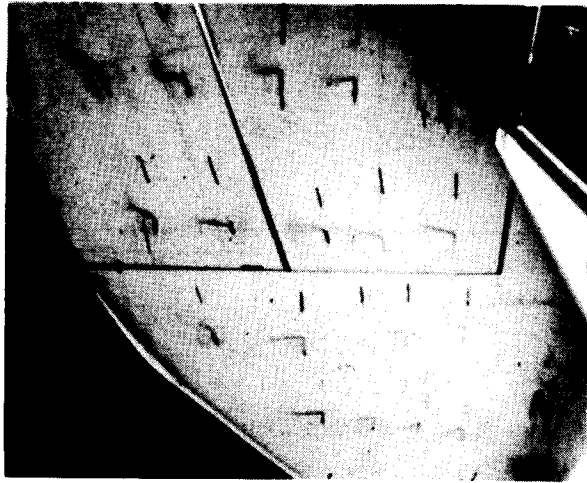


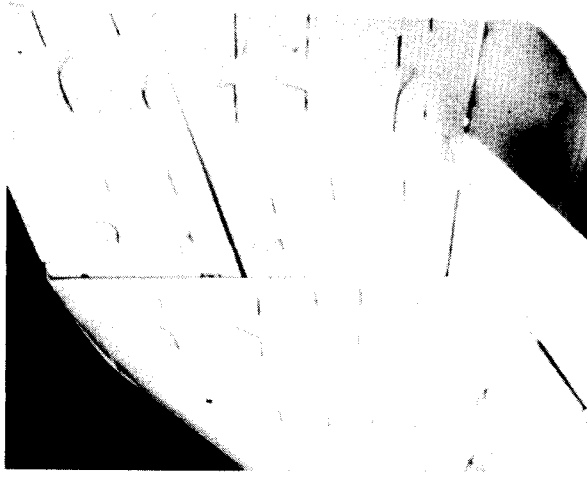
Figure 12. Variation of the lower-flap hinge-moment coefficient due to lower-flap deflection as a function of Mach number .



(a) Chordwise flow. E-24555



(b) Spanwise flow. E-24671



(c) Separated flow. E-24672

Figure 13. In-flight photos of tufts on the inboard surface of the right fin.

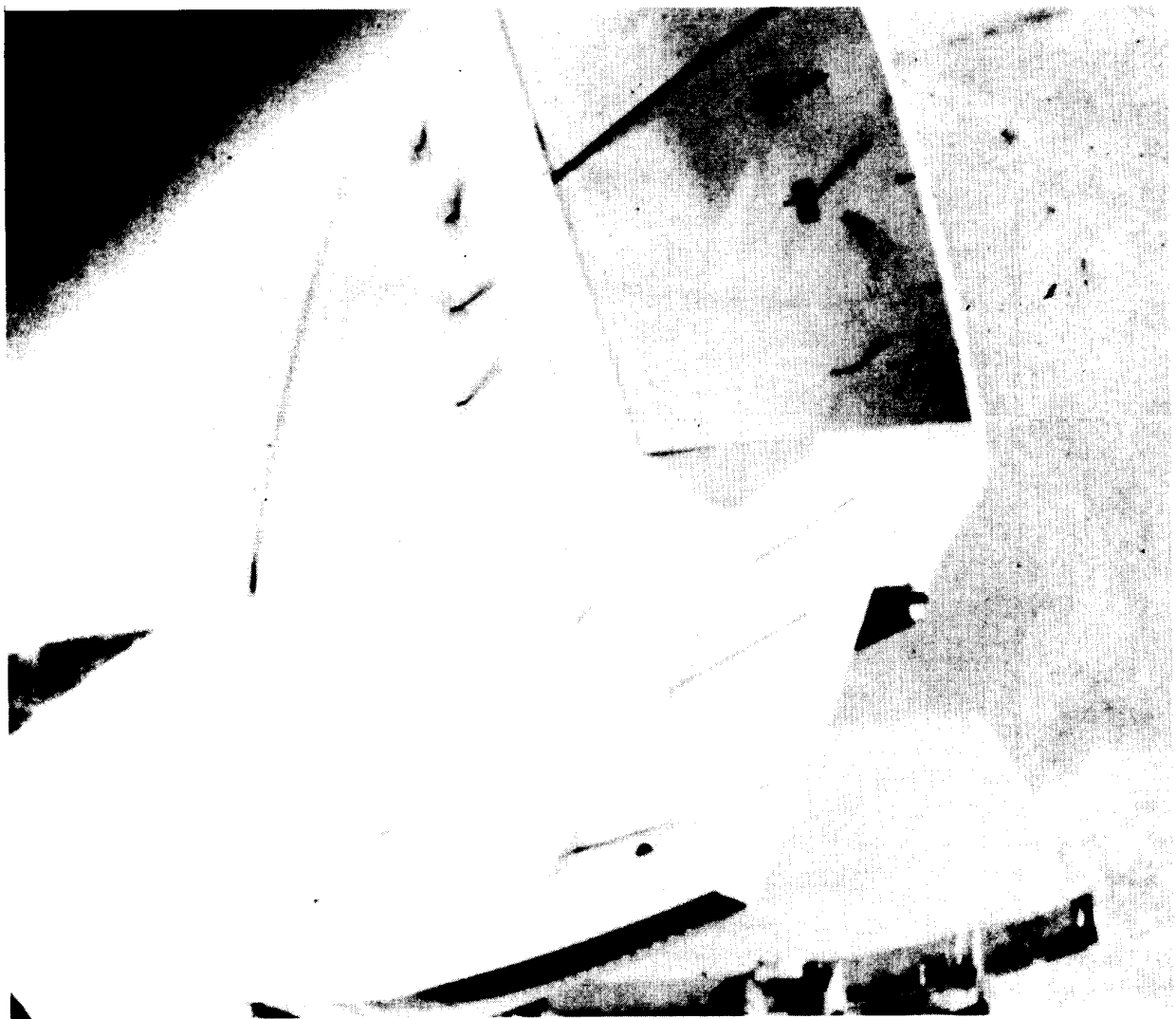


Figure 14. In-flight photo of tufts on the right upper flap and right fin. E-24558

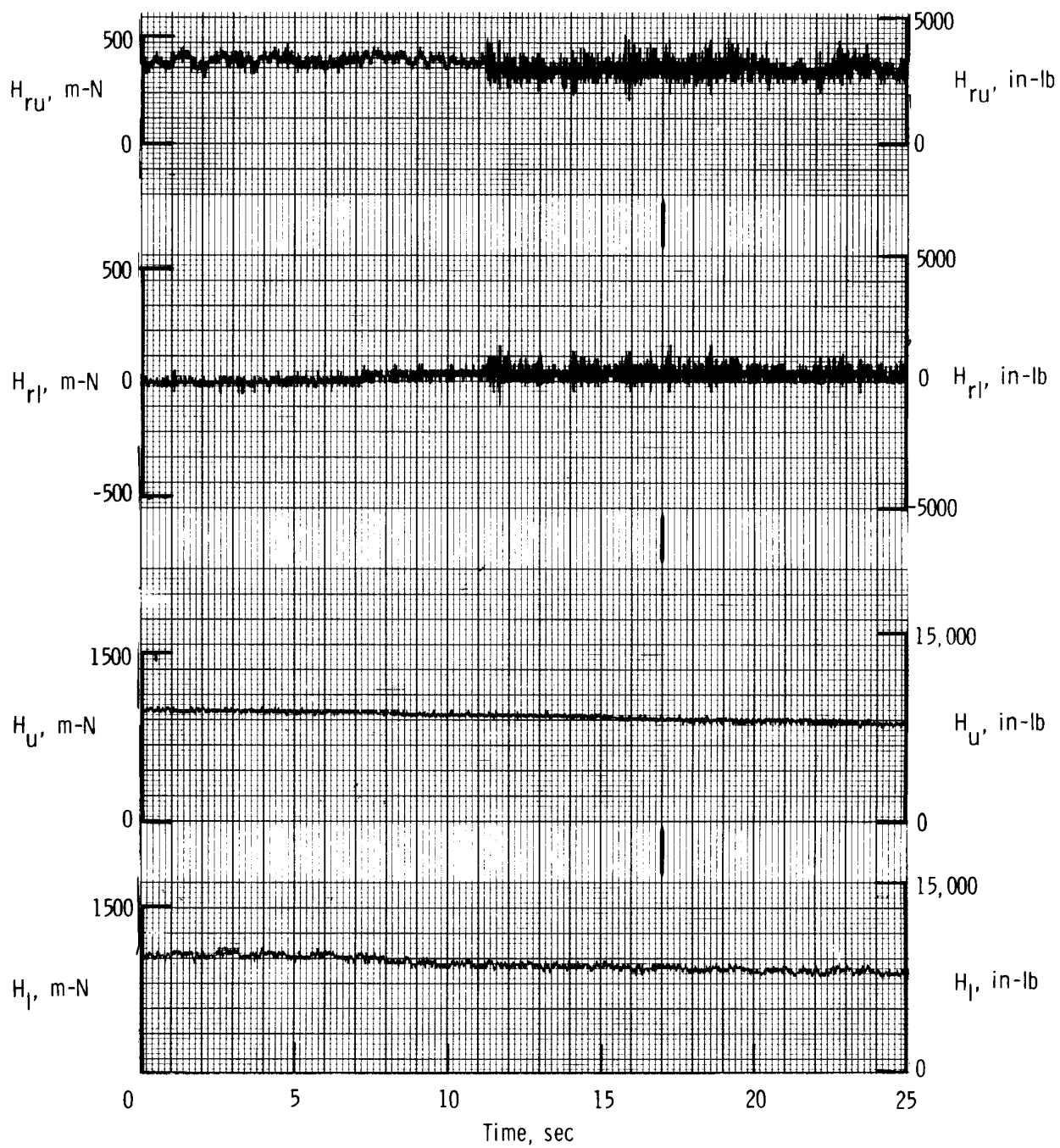


Figure 15. Time history of right control-surface hinge-moment strain-gage responses during flight.

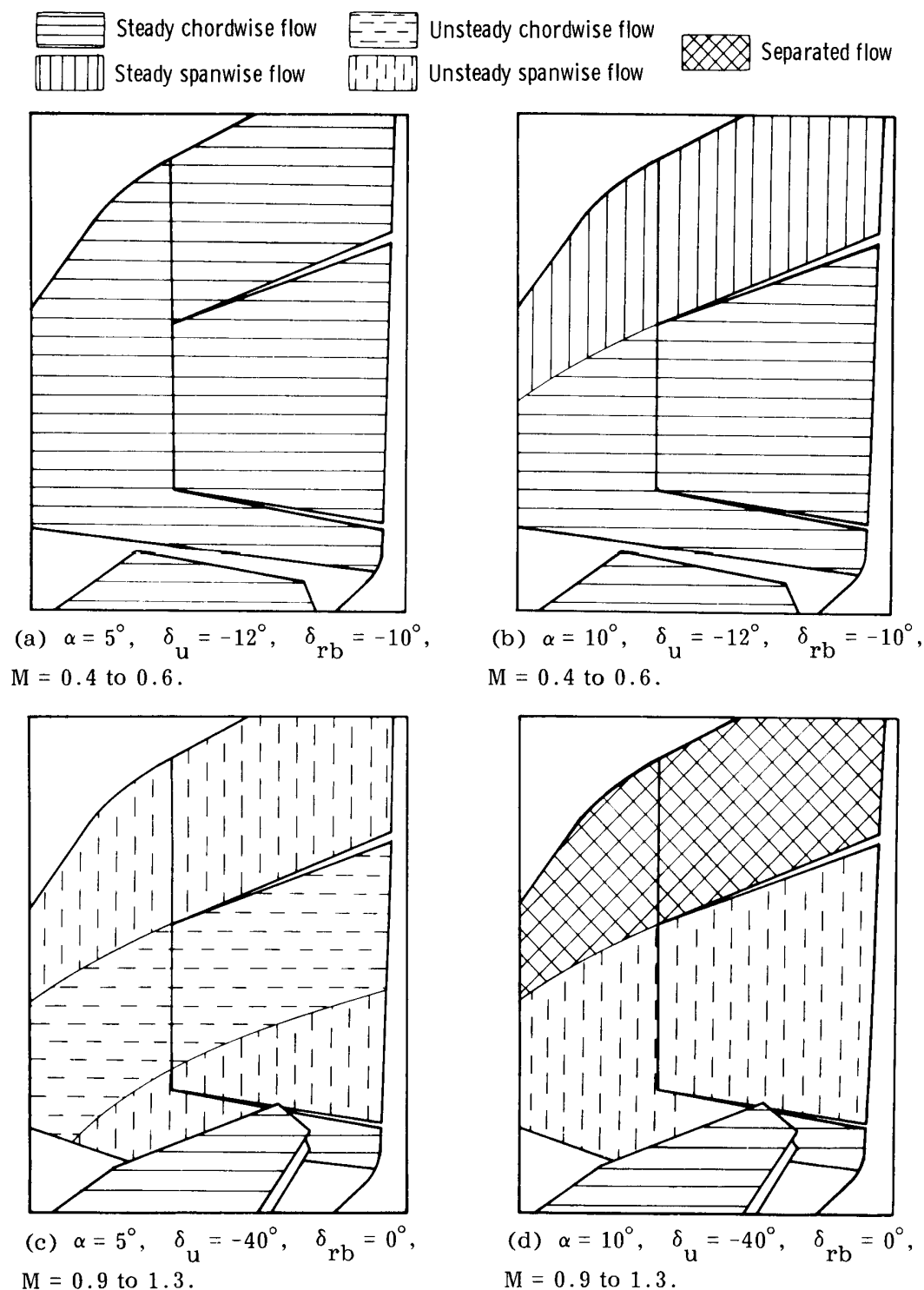


Figure 16. Flow conditions on the inboard surface of the right fin and right upper flap as determined from in-flight tuft photos.